Handbook of

9

THEORETICAL and COMPUTATIONAL NANOTECHNOLOGY

Nanocomposites, Nano-Assemblies, and Nanosurfaces

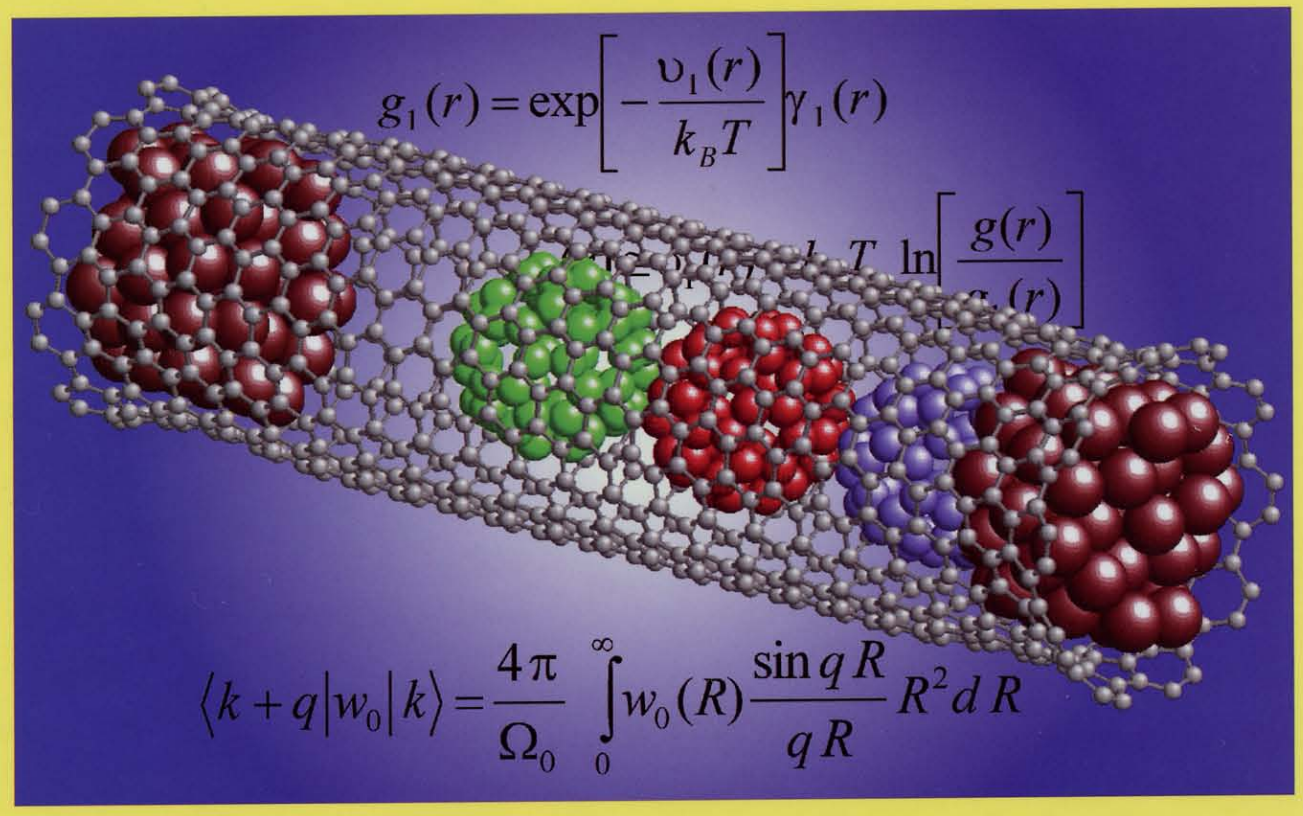

Edited by

Michael Rieth and **Wolfram Schommers**

Foreword by

Pierre-Gilles de Gennes, Nobel Prize Laureate

ASP
AMERICAN SCIENTIFIC PUBLISHERS

CHAPTER 10

Electronic Properties and Reactivity of the Doped and Defected Single-Walled Carbon Nanotubes

Wei Quan Tian, Lei Vincent Liu, Yan Alexander Wang*

Department of Chemistry, University of British Columbia, Vancouver, British Columbia, Canada

CONTENTS

ISBN: 1-58883-051-9

Handbook of Theoretical and Computational Nanotechnology
Edited by Michael Rieth and Wolfram Schommers
Volume 9: Pages (499–524)

1. INTRODUCTION

Since the discovery of the single-walled carbon nanotube (SWCNT) [1], experimental and theoretical investigations on the chemical [2, 3] and physical [4, 5] properties of SWCNTs have been growing rapidly because of the potential applications [6] of SWCNTs in molecular electronics [7], chemical sensor [8], vacuum electronic devices [9], field-emission flat-panel display [10], catalysis [11], and optics [12].

The SWCNT can be visualized as a roll of graphite sheet and can be metallic and semiconducting nanotubes according to the wrapping vectors (m, n) [13]. Semiconducting nanotubes can be further classified as narrow-gap and moderate-gap semiconductors. A nanotube is characterized by its chiral vector (**AB** as shown in Scheme 1), $\mathbf{AB} = ma + nb$, and a translation vector in which the nanotube elongates. In the (5,5) nanotube as shown in Scheme 1, the translation vector is in the y-axis. If $n - m = 3q$ (with an integer q), then the nanotube is metallic; otherwise, the nanotube is semiconducting with a band gap [13b]. There are further detailed classifications of nanotubes with respect to conductance according to the "$n - m$ rules" [13]. As rolled one-dimensional graphite sheet, nanotubes display different electronic properties from those of graphite sheets and fullerenes: the electronic properties of nanotubes can be controlled by the diameters of the nanotubes because of hybridization effects [5a]. The pyramidalization of nanotubes is different from fullerenes, and there exists π-orbital misalignment between adjacent pairs of conjugated carbon atoms [2a], which renders different reactivities of nanotubes from fullerenes and among nanotubes themselves because of different diameters [2a, 5e, 14]. Chemical reactions can take place on the sidewall of nanotubes [15] or at the end of nanotubes [2d, 15j, 15k, 16]. Because of the difficulty in purifying and manipulating SWCNTs, the electronic structure, chemical reactivity, and possible applications of SWCNTs are waiting for further investigation. Especially, the reactivity of SWCNTs is still not clear in spite of numerous attempts, and it deserves further studies [17].

The partial destruction of the nanotube structure through vacancy [18], doping [19], and distortion [20] can alter the electronic structure and reactivity of nanotubes [18g, 19c]. In doping, some carbon atoms on a SWCNT are replaced by different atoms, producing a hetero-SWCNT (HSWCNT) [19]. Most HSWCNTs are doped with main group elements [19]; the HSWCNT we study here is doped with precious metal Pt. The substitution of a metal atom in fullerenes [21] prepares the metal as an active center in chemical reactions [21e, 22].

A good understanding of the electronic structure of SWCNTs and defected SWCNTs offers deep insight into the reactivity of SWCNTs and paves the way for a general utilization of SWCNTs in chemical reactions. As a pseudo–one-dimensional system with a tube

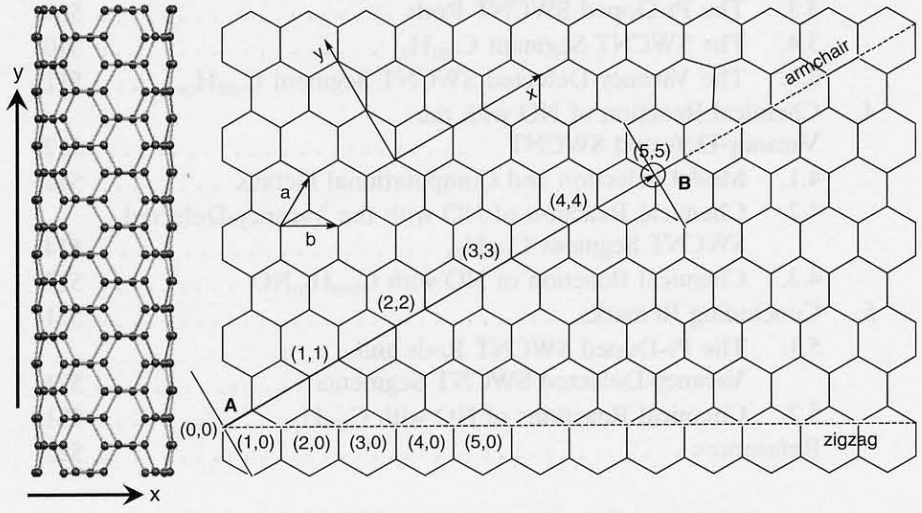

Scheme 1. Illustration of possible wrapping of graphite sheet to form the SWCNTs. The structure of the (5,5) SWCNT is shown on the left. The x-axis is the wrapping direction, the y-axis is the elongation direction, and **AB** is the chiral vector.

structure, a SWCNT with defect can sever as a catalyst for gas- and liquid-phase reactions: the reactants are fed from one end of an open SWCNT, the reaction is catalyzed on the defect site of the SWCNT, and the products are released from the other end of the SWCNT. HSWCNTs can also be used in gas sensors because of the chemical activity of the doped heteroatoms. B- and N-doped HSWCNTs attracted extensive attentions due to their potential applications in chemical sensors [19c] and nanosize electronic and photonic devices with various electronic properties [23].

For the time being, the synthetic methods for these HSWCNTs, such as thermal treatment [24] or the chemical vapor deposition [25], can only work under very high temperatures of hundreds and thousands of degrees and the position where the heteroatom is doped cannot be controlled with ease. The feasibility of such synthesis under mild conditions has not been explored theoretically nor reported experimentally.

However, the rapid development of theoretical methods makes computational studies on the structure and property of SWCNTs possible, shedding light on possible applications of SWCNTs. However, this does not claim that theoretical approaches will be easy in any way. The size of SWCNTs lies between small molecule and bulky particle in the range of the so-called nanosize, which is too big for accurate quantum mechanical treatment (for capturing quantum effect) and too small for bulky calculations (for macroscopic properties). The quantum effect of nanosize particles is important in studying their properties; this very fact necessitates the application of quantum mechanical treatment for nanosize materials.

In this work, we will study the structure of HSWCNTs, electronic properties of SWCNT clips, capped SWCNTs, SWCNT clip with vacancy defect, and chemical reaction of the vacancy-defected SWCNT with nitrogen monoxide (NO) gas to explore the feasibility of synthesis of the HSWCNT from the SWCNT with vacancy.

2. QUANTUM MECHANICAL METHODS

2.1. First-Principles Calculations

Quantum mechanical methods can be carried out for a system by solving the electronic Schrödinger equation,

$$\mathbf{H}_e \Psi = E\Psi \tag{1}$$

under the adiabatic approximation, in which the electronic wave function is restricted to one electronic surface, and the Born-Oppenheimer approximation that warrants the separation of the nuclear and electronic motions since the nuclei move much slower than the electrons [26]. The electronic Hamiltonian $\mathbf{H}_e$,

$$\mathbf{H}_e = \mathbf{T}_e + \mathbf{V}_{ne} + \mathbf{V}_{ee} \tag{2}$$

includes the electronic kinetic energy $\mathbf{T}_e$, nucleus–electron attraction $\mathbf{V}_{ne}$, and electron–electron interaction $\mathbf{V}_{ee}$. The total Hamiltonian $\mathbf{H}_{tot}$ includes $\mathbf{H}_e$, the nuclear kinetic energy $\mathbf{T}_n$, and nucleus–nucleus interaction $\mathbf{V}_{nn}$,

$$\mathbf{H}_{tot} = \mathbf{H}_e + \mathbf{T}_n + \mathbf{V}_{nn} \tag{3}$$

In most quantum mechanical methods, the nuclei are treated as classical particles and only the electronic wave function is solved quantum mechanically. If only fundamental physical constants are used in solving the electronic Schrödinger equation, first-principles calculation emerges. On the basis of the choice of the basic variational variables, first-principles calculation has two flavors: wave function-based *ab initio* methods [26] and electron-density-based density-functional theory (DFT) [27]. In wave function-based *ab initio* methods, the electronic energy of a system can be expressed as

$$\mathbf{E}_e[\Psi] = \mathbf{T}_e[\Psi] + \mathbf{V}_{ne}[\Psi] + \mathbf{V}_{ee}[\Psi] \tag{4}$$

In the quasi-independent-particle models, for example, the Hartree-Fock (HF) method [26] and the Kohn-Sham (KS) method [27], the electronic wave function is approximated by a single Slater determinant for an N-electron system,

$$\Psi = \frac{1}{\sqrt{N!}} \begin{vmatrix} \chi_1(1) & \chi_2(2) & \cdots & \chi_N(1) \\ \chi_1(2) & \chi_2(2) & \cdots & \chi_N(2) \\ \vdots & \vdots & \ddots & \vdots \\ \chi_1(N) & \chi_2(N) & \cdots & \chi_N(N) \end{vmatrix} \tag{5}$$

where χ_i is the ith spin orbital. Because of the quasi-independent-particle nature, the instantaneous multielectron interaction is approximated as if an electron is moving in an average electron–electron potential because of other electrons in the system. The variational HF (or KS) equation is solved self-consistently with a basis set representation for molecular orbitals (MOs), which are usually constructed from the linear combination of atomic orbitals (LCAOs) [26–28].

The HF approximation is not capable of describing highly correlated systems, in which the instantaneous electron–electron interaction is crucial to describe correctly the electronic structure. High-level theories, such as multiconfiguration self-consistent field (MCSCF) [29], multireference configuration interaction (MRCI) [30], or coupled-cluster (CC) methods [31], are then necessary for treating the electron correlation more accurately. However, the prohibitive computing resource requirements of such high-level methods prevent their general application in large systems [26]. Even for the HF approximation, the system size that can be treated is still moderate, because the computational cost formally scales as the fourth power of the number of basis functions. High-level theory, such as CC, scales even worse with respect to the system size. One solution to reduce the computing cost is developing linear-scaling methods. Another way is reducing the computing requirements by approximating the most time-consuming aspect of the calculation, evaluating the two-electron integrals. This latter approximation results in semiempirical methods [26].

2.2. Semiempirical Quantum Mechanical Methods

In the HF approximation, the electron–electron interaction is evaluated through the operator $\mathbf{V}_{ee}$,

$$\mathbf{V}_{ee} = \sum_{i}^{N} \sum_{j>i}^{N} \frac{1}{|\mathbf{r}_i - \mathbf{r}_j|} \tag{6}$$

which results in the two-electron integrals. By linear combination of atomic basis functions $\{\varphi_a\}$, the molecular orbitals $\{\chi_i\}$ can be written as

$$\chi_i = \sum_a c_{ai} \varphi_a \tag{7}$$

Following the variation principle, the HF equation can be derived directly from Eqs. (1), (2), and (5) as a pseudo–one-electron eigenequation:

$$\mathbf{F}\chi_i = \varepsilon_i \chi_i \tag{8}$$

where $\mathbf{F}$ is the Fock operator. In the atomic basis function representation, the HF equation is recasted as the Roothaan-Hall equations,

$$\mathbf{FC} = \mathbf{SC}\boldsymbol{\varepsilon} \tag{9}$$

where $\mathbf{F}$ is the Fock operator matrix, $\mathbf{C}$ is the MO coefficient matrix, and $\mathbf{S}$ is the overlap matrix, respectively. The Fock operator $\mathbf{F}$ could be written as a sum of one-electron operator $\mathbf{h}$ and two-electron operators

$$\mathbf{F} = \mathbf{h} + \sum_{j}^{N} (\mathbf{J}_j - \mathbf{K}_j) \tag{10}$$

where $\mathbf{J}_j$ is the Coulomb operator and $\mathbf{K}_j$ is the exchange operator for two-electron interactions, respectively. Most of the CPU time is spent in calculating the two-electron integrals due to the two-electron operators $\mathbf{J}_j$ and $\mathbf{K}_j$ [26].

In semiempirical methods [26c–26e], only valence electrons are considered explicitly; the core electrons are implicitly included in the nuclear part by reducing the nuclear charge. The evaluation of the two-electron integrals for valence electrons is simplified by the introduction of parameters. To further reduce the computational cost, only a minimum number of basis functions are introduced to describe the motion of electrons in semiempirical methods. The basic approximation in semiempirical methods is the zero differential overlap (ZDO) approximation, in which all the products of basis functions of the same electron on different atoms are neglected. The remaining integrals are parameterized and fitted through benchmarking with available experimental data. Different semiempirical methods emerged depending on how the approximations in the neglect of two-electron integrals and in the fitting of parameters are made [26c–26e]. Among all variants of the ZDO approximation, the complete neglect of differential overlap (CNDO) method [32] is the crudest approximation. In the CNDO method, only Coulomb one-center and two-center two-electron integrals remain. With more refined ZDO approximation, the intermediate neglect of differential overlap (INDO) method [33] and the neglect of diatomic differential overlap (NDDO) methods [32] (MNDO [34], AM1 [35], and PM3 [36]) emerged with much-improved accuracy. In this work, the PM3 method is employed in combined quantum chemical calculations.

2.3. Density-Functional Theory

In conventional *ab initio* methods, the computational cost scales formally at least as the fourth power of the number of basis functions. To incorporate electron correlation effects into the HF approximation, high-level theory has to pay a big price in terms of computational cost. However, the electron-density-based DFT has a favorable scaling factor [26, 27]: the third power of the number of basis functions in the KS scheme, and more importantly, the electron correlation effects are taken into account through exchange-correlation functionals in DFT [27].

In DFT, the electronic energy is expressed as a sum of various energy density functionals,

$$E_e[\rho] = T_s[\rho] + E_{ne}[\rho] + J[\rho] + E_{xc}[\rho] \tag{11}$$

where ρ is the single-electron density. $T_s[\rho]$ is the electronic kinetic energy, $E_{ne}[\rho]$ is the nuclear–electron attraction, $J[\rho]$ is the electron–electron Coulomb interaction, and $E_{xc}[\rho]$ is the exchange and correlation energy. The $E_{xc}[\rho]$ term can be split into two pieces: the exchange energy $E_x[\rho]$ and the correlation energy $E_c[\rho]$.

The $E_{xc}[\rho]$ functionals are mainly modeled in three ways: the local-density approximation (LDA), the generalized gradient approximation (GGA), and the hybrid approach [27, 37]. In the LDA, the energy of a system depends on the local value of the electron density [27]. In the GGA, the energy of a system depends not only on the local value of the electron density but also on the gradients of the electron density of different orders [27d]. While in the hybrid DFT, the exact exchange defined in terms of the KS orbitals (just like the one used in the HF approximation defined in terms of the HF orbitals) is admixed [38]. Such a hybrid approach of mixing the exact exchange further improves the prediction accuracy of DFT method in physical and chemical applications [38].

However, the system size and scaling factor of computational cost limit the application of quantum mechanical methods in the studies of nanoparticles. To overcome this difficulty, the ONIOM model [39] has been developed to be a compromise of the computational feasibility and accuracy.

2.4. ONIOM Model

In most cases, chemical reactions are localized in the proximity of the active site. Such a localized nature of chemical reactions legitimizes an accurate treatment of the active site with high-level theory, while the surroundings (the rest of the chemical system) can be treated with low-level theory [39, 40]. This embedding approach requires relatively low computing resources and still keeps the essential environmental effects exerted on the active site by the surroundings [40].

The ONIOM model [39] is a popular one among many methods [40] suitable for such applications. The basic formula for ONIOM can be written as [39],

$$E_{\text{total}} = E_{\text{RL}} - E_{\text{ML}} + E_{\text{M}_\text{H}} \tag{12}$$

where E_{total} is the total energy of the system, E_{RL} is the energy of the real system at low-level theory, E_{ML} is the energy of the model system (the active site) at low-level theory, and E_{MH} is the energy of the model system at high-level theory. The gradient and the second-order derivatives of the total energy with respect to the nuclear coordinates can be calculated in a similar manner with the help of link atoms [39]. The link atom is a buffer atom in the model system replacing the actual atom in the real system connected to the model system.

For very large systems, the low-level theory for the overall real system is usually molecular mechanics. In molecular mechanics [26], the electronic structure of the system is not explicitly considered. The interatomic interactions are divided into bond, angle, torsion angle, and weak interactions, including the van der Waals interaction. Such interactions are parameterized through fitting to the available experimental data or any high-level quantum mechanical calculation results. Depending on the fitting procedure, different parameterizations give rise to various force fields for the interatomic interactions. The most popular force fields are Amber [41], Charmm [42], MM3 [43], UFF [44], and so on [26].

3. SINGLE-WALLED CARBON NANOTUBES

3.1. Models and Computational Details

The model for the SWCNT used in present work is the metallic armchair (5,5) SWCNT. Two different models are chosen for a finite-length (5,5) SWCNT: the hemispherically capped nanorod and the hydrogen saturated open-end SWCNT. The caps in the hemispherically capped nanorod are half spheres of a fullerene. The open ends of the SWCNT were found to be active centers in many reactions, e.g., the oxidation of the SWCNT [2d], and the structure of the open ends goes through bond-distance reconstruction [3i]. No end-localized state has been found near the Fermi energy for the open-end SWCNT [3i]. On the contrary, the caps in capped nanorod were predicted to be important to the electronic property of the nanorod [3d]. The caps host some localized electronic states [4a, 45], because of the relatively unstable pentagons presented there [46]; however, there is no significant contributions to the highest-occupied molecular orbital (HOMO) and the lowest-unoccupied molecular orbital (LUMO) of the nanorods from the caps [3c]. The differences in curvature and π bonding distinguish the chemical properties of fullerenes and SWCNTs [2a] and thus divide the nanorod into at least two regions: the caps and the sidewall.

All the calculations are performed with the Gaussian 03 quantum chemical package [47]. Becke's exchange functional (B) [38] and Perdew's correlation functional (PW91) [48] of the GGA type are employed in structure optimization and property prediction. Pople's 6-31G Gaussian basis set [49] is used for the carbon atoms and the relativistic 19-electron Los Alamos National Laboratory effective core pseudopotential (LANL2DZ) [50] and its corresponding valence-electron basis set ($3s3p2d$) are used for the Pt atom. The geometries of the open-end (5,5) SWCNTs, with and without vacancy defect, are optimized with PM3. Partial charge analysis within natural bond orbitals (NBOs) [51] and molecular orbitals are calculated with the BPW91 functionals and with the 6-31G basis set for all structures.

3.2. The Unsubstituted SWCNT Rod

Figures 1 and 2 display the geometries, density of states (DOS), and local density of states (LDOS) of two (5,5) SWCNT rods, C_{170} with D_{5h} symmetry and C_{180} with D_{5d} symmetry, respectively. The overall DOS and LDOS of these two SWCNT rods are very similar. The most noticeable feature of the DOS of C_{170} is the separation of peaks at 5.2 eV, where it is continuous for C_{180}. The similarity of the DOS and LDOS of C_{170} and C_{180} is expected, because only one additional circular *cis*-polyene chain does not change the electronic structure significantly from C_{170} to C_{180}. Previous studies also found the similarity in the HOMO-LUMO gaps of the (5,5) SWCNT rods C_{170} and C_{180} [3d]. The HOMO-LUMO gaps of the

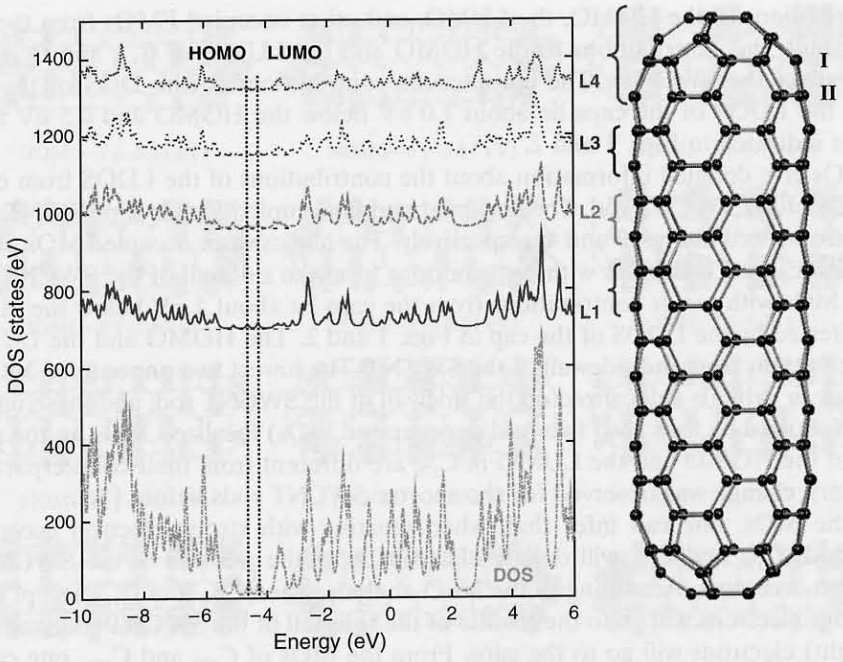

Figure 1. The density of states and local density of states for the nanorod C_{170} with D_{5h} symmetry. HOMO (−4.61 eV) is the highest-occupied molecular orbital and LUMO (−4.26 eV) is the lowest-unoccupied molecular orbital. L1, L2, L3, and L4 are the local density of states for each specified layer of C_{170} as outlined on the structure.

(5,5) SWCNT rods C_{170} and C_{180} are smaller than that of the longer open-end (5,5) SWCNT segment (this will be elaborated in next section). The LDOS shows the contribution of a particular group of atoms to the overall DOS. Figures 1 and 2 display the LDOS of *cis*-polyene chains in C_{170} and C_{180} along the SWCNT axis and the LDOS of the cap (a hemisphere of C_{60}). The shapes of the LDOS of different layers are similar at the frontier molecular orbital (FMO) region, which indicates the delocalization of the FMOs of the SWCNT rod.

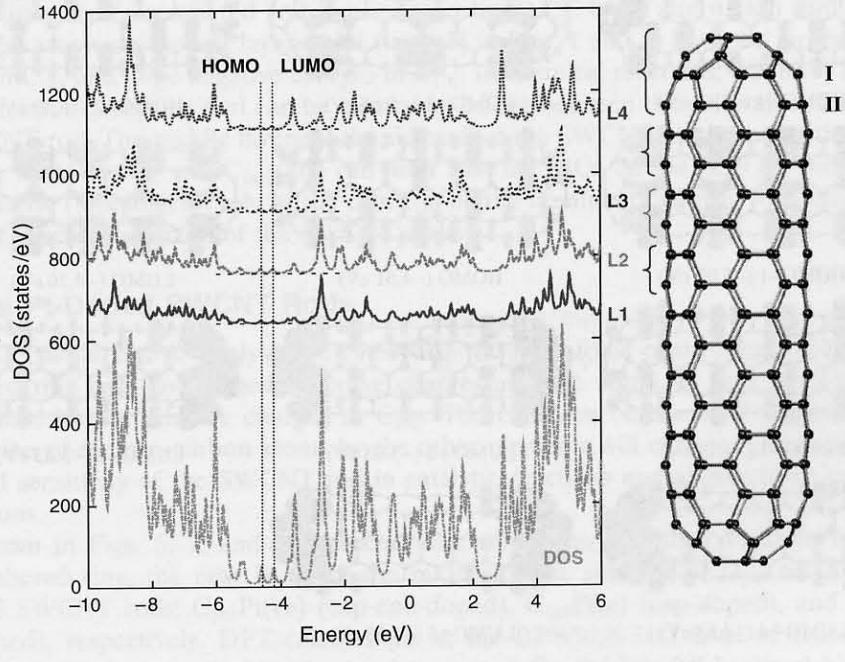

Figure 2. The density of states and local density of states for the nanorod C_{180} with D_{5d} symmetry. HOMO (−4.60 eV) is the highest-occupied molecular orbital and LUMO (−4.23 eV) is the lowest-unoccupied molecular orbital. L1, L2, L3, and L4 are the local density of states for each specified layer of C_{180} as outlined on the structure.

The contributions to the HOMO, the LUMO, and other occupied FMOs from the caps are not significant; the contributions to the HOMO and the LUMO of C_{170} and C_{180} are from the sidewall of the SWCNTs. The conspicuous contributions to the DOS of the SWCNT rod from the LDOS of the caps lie about 1.0 eV below the HOMO and 0.5 eV above the LUMO as indicated in Figs. 1 and 2.

The MOs give detailed information about the contributions of the LDOS from each layer to the DOS of the SWCNT rod. The occupied and unoccupied FMOs for SWCNT rods C_{170} and C_{180} are plotted in Figs. 3 and 4, respectively. The highest four occupied MOs of C_{170} and C_{180} are delocalized π orbitals with contributions from the sidewall of the SWCNT rod. The occupied MOs with major contributions from the caps lie about 1 eV below the HOMO, as also manifested by the LDOS of the cap in Figs. 1 and 2. The HOMO and the LUMO have sole contributions from the sidewall of the SWCNT. The lowest two unoccupied MOs of C_{170} and C_{180} are π orbitals delocalized on the sidewall of the SWCNT rod, and these unoccupied MOs are followed by four (two two-fold degenerated MOs) localized MOs on the caps. The patterns of the HOMO and the LUMO in C_{170} are different from their counterparts in C_{180}. Such pattern change was observed for the shorter SWCNT rods before [3c].

From the MOs, one can infer that, when reacting with strong electron acceptors, the SWCNT rods C_{170} and C_{180} will donate electrons from the sidewall of the SWCNT rod to the electron acceptors. According to the NBO analysis, when C_{170} and C_{180} accept electrons, the first four electrons will go to the middle of the sidewall of the SWCNT rod, and any extra (up to eight) electrons will go to the caps. From the MOs of C_{170} and C_{180}, one cannot see clearly the separation of the cap from the sidewall, though there are some gradual geometric changes from the cap to the sidewall of the SWCNT rod [52]. The delocalized MOs on the sidewall of the SWCNT rod extend to the ridge of the five-membered rings of the caps.

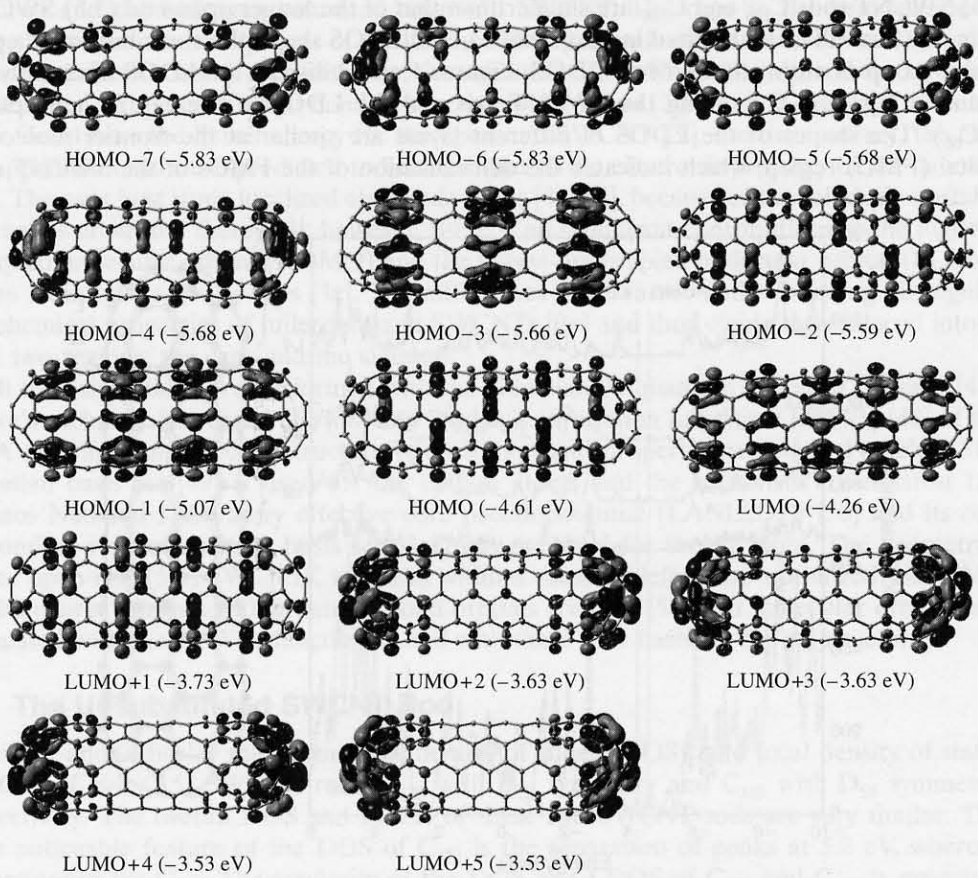

Figure 3. The frontier molecular orbitals of the nanorod C_{170} with D_{5h} symmetry. HOMO–n (p eV) is the nth orbital below the HOMO with orbital energy p eV. LUMO + m (q eV) is the mth orbital above the LUMO with orbital energy q eV.

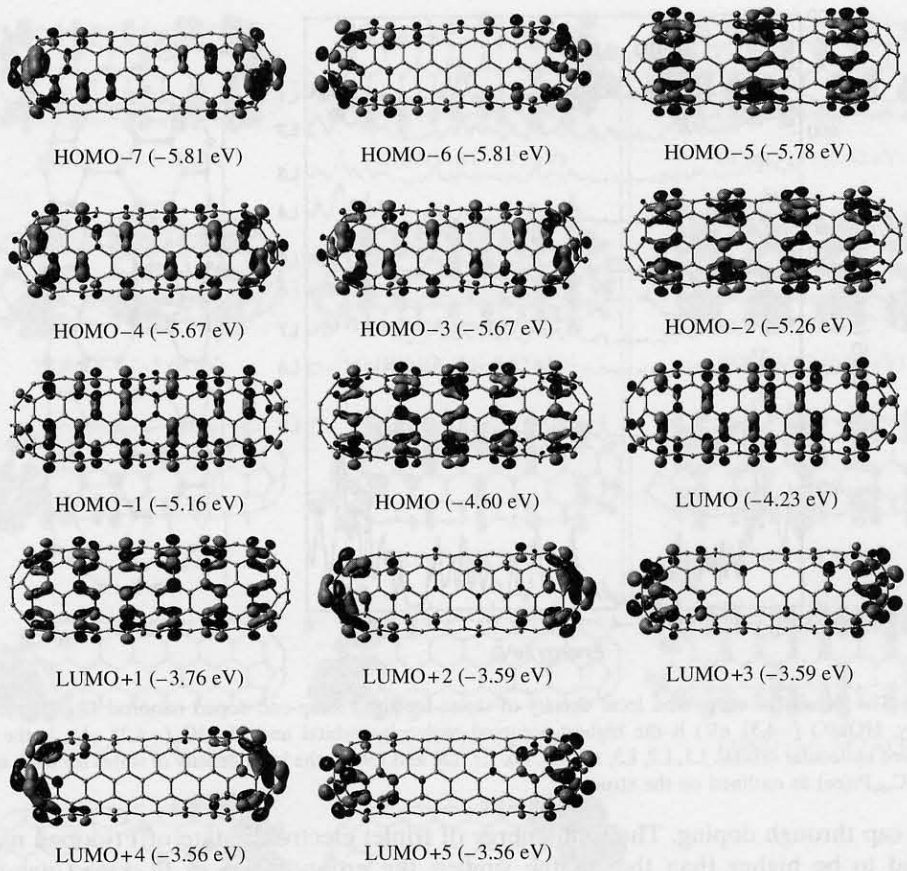

Figure 4. The frontier molecular orbitals of the nanorod C_{180} with D_{5d} symmetry. HOMO–n (p eV) is the nth orbital below the HOMO with orbital energy p eV. LUMO+m (q eV) is the mth orbital above the LUMO with orbital energy q eV.

The five-membered ring regions have 6–6 (between 6-membered and 6-membered rings) and 6–5 (between 6-membered and 5-membered rings) CC bond alternation similar to that in C_{60}. The atoms on the last layer of L4 (layer **II** in Figs. 1 and 2) have the largest negative charges in C_{180} and large negative charges in C_{170}. In chemical reactions, this layer is reactive toward electron acceptors and can be treated as bridge between the sidewall and the cap of the SWCNT rod. The middle layers of the sidewall of the SWCNT rod have positive charges. From the MOs of C_{170} and C_{180}, one can infer that the MOs on the caps are localized and the geometric (topological) role of the caps can be the dominant factor in the determination of the electronic properties of the SWCNT rods.

3.3. The Pt-Doped SWCNT Rods

The NBO partial charge analysis indicates that the five atoms connecting to the top five-membered ring cap have largest negative charges and the atoms of next layer (layer **I** in Fig. 1) have largest positive charges in C_{170}. The caps can be chemical reaction centers. Substitution of the cap carbon atoms by the other elements will change the chemical selectivity and sensitivity of the SWCNT rod in catalytic reactions and atomic force microscopy applications.

As shown in Figs. 5, 7, and 9, replacing one carbon atom with a Pt atom in the end five-membered ring, the next layer, or the middle of the sidewall of C_{170} results in three Pt-doped SWCNT rods: $C_{169}Pt$(**ce**) (cap-end-doped), $C_{169}Pt$(**c**) (cap-doped), and $C_{169}Pt$(**w**) (wall-doped), respectively. DFT calculations at the BPW91/6-31G level of theory predict $C_{169}Pt$(**ce**) to be the most stable: the total energy of $C_{169}Pt$(**c**) is 0.8 kcal/mol higher than that of $C_{169}Pt$(**ce**) and $C_{169}Pt$(**w**) is 17.9 kcal/mol above $C_{169}Pt$(**ce**). Evidently, the cap-doped SWCNT is more stable than the wall-doped SWCNT due to the relaxation of the constraint

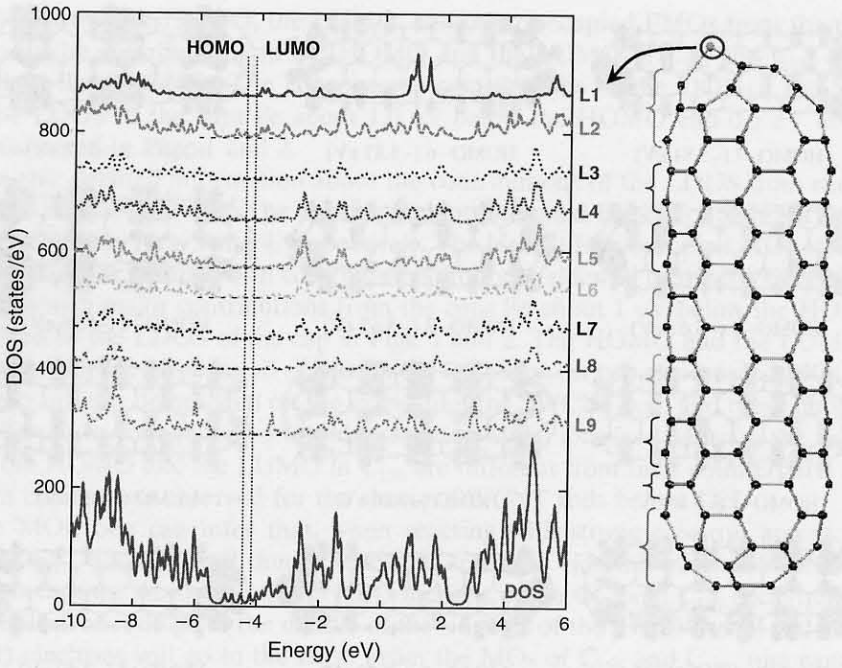

Figure 5. The density of states and local density of states for the Pt cap-end-doped nanorod $C_{169}Pt(\mathbf{ce})$ with C_s symmetry. HOMO (−4.51 eV) is the highest-occupied molecular orbital and LUMO (−4.21 eV) is the lowest-unoccupied molecular orbital. L1, L2, L3, L4, L5, L6, L7, L8, and L9 are the local density of states for each specified layer of $C_{169}Pt(\mathbf{ce})$ as outlined on the structure.

on the cap through doping. The total energy of triplet electronic state of Pt-doped nanorod is found to be higher than that of the singlet: the ground state of Pt-doped nanorod is singlet. Moreover, present studies find that the change of structure and reactivity through the doping of Pt in SWCNT is localized at the doping site.

3.3.1. $C_{169}Pt(ce)$

Figures 5 and 6 display the structure, DOS, LDOS, and MOs of $C_{169}Pt(\mathbf{ce})$. The Pt–C (of the cap end) bond distances are about 2.01 Å and the other Pt–C bond distances are about 1.96 Å. Clearly, the Pt atom points outwards along the translational direction of the SWCNT. The distortion of the SWCNT rod due to the doping of Pt is localized in the pentagons and hexagons around Pt. The overall DOS of $C_{169}Pt(\mathbf{ce})$ is similar to that of the SWCNT C_{170} with D_{5h} symmetry. The doping of Pt produces more peaks around the FMO region of the DOS due to the introduction of the $5d$ orbitals of Pt and induces electronic structure changes of the cap with the Pt-doping. The LDOS of **L1** and **L2** in Fig. 5 clearly indicate such changes in the electronic structure. **L1** (the LDOS of Pt) in Fig. 5 manifests the contribution of Pt to the DOS of the Pt-doped SWCNT rod. The LDOS of the remaining layers in Fig. 5 are similar. The FMOs in Fig. 6 reveal details of the electronic structure of $C_{169}Pt(\mathbf{ce})$. The HOMO of $C_{169}Pt(\mathbf{ce})$ is similar to that of C_{170}, except for some significant contributions from Pt and its neighboring carbon atoms in $C_{169}Pt(\mathbf{ce})$. The effect of Pt on the electronic structure of $C_{169}Pt(\mathbf{ce})$ is also reflected in occupied MOs: the HOMO–1, the HOMO–5, the HOMO–6, and the HOMO–7. The HOMO–1 has some major contributions from the $5d$ orbitals of Pt, which form d-p π bonds with the carbon atoms in the next layer. The geometric distortion in $C_{169}Pt(\mathbf{ce})$ induces single- and double-CC bond alteration around Pt, which is reflected in the HOMO–5 as the strong π bonding around the cap with doping. The symmetry of the π bonds in the HOMO–7, the HOMO–6, and the HOMO–5 (corresponding to the HOMO–7, the HOMO–6, and the HOMO–5 in C_{170}) is destroyed in $C_{169}Pt(\mathbf{ce})$, resulting in the concentration of π bonding on one end cap as shown in Fig. 6. The LUMO in $C_{169}Pt(\mathbf{ce})$ is very similar to that in the SWCNT rod C_{170}. The LUMO+1 in C_{170} corresponds to the LUMO+3 (with contribution from Pt) in $C_{169}Pt(\mathbf{ce})$. The two unoccupied MOs, the LUMO+1 and the LUMO+2, in $C_{169}Pt(\mathbf{ce})$ are mainly from the $5d$ orbitals of Pt, and

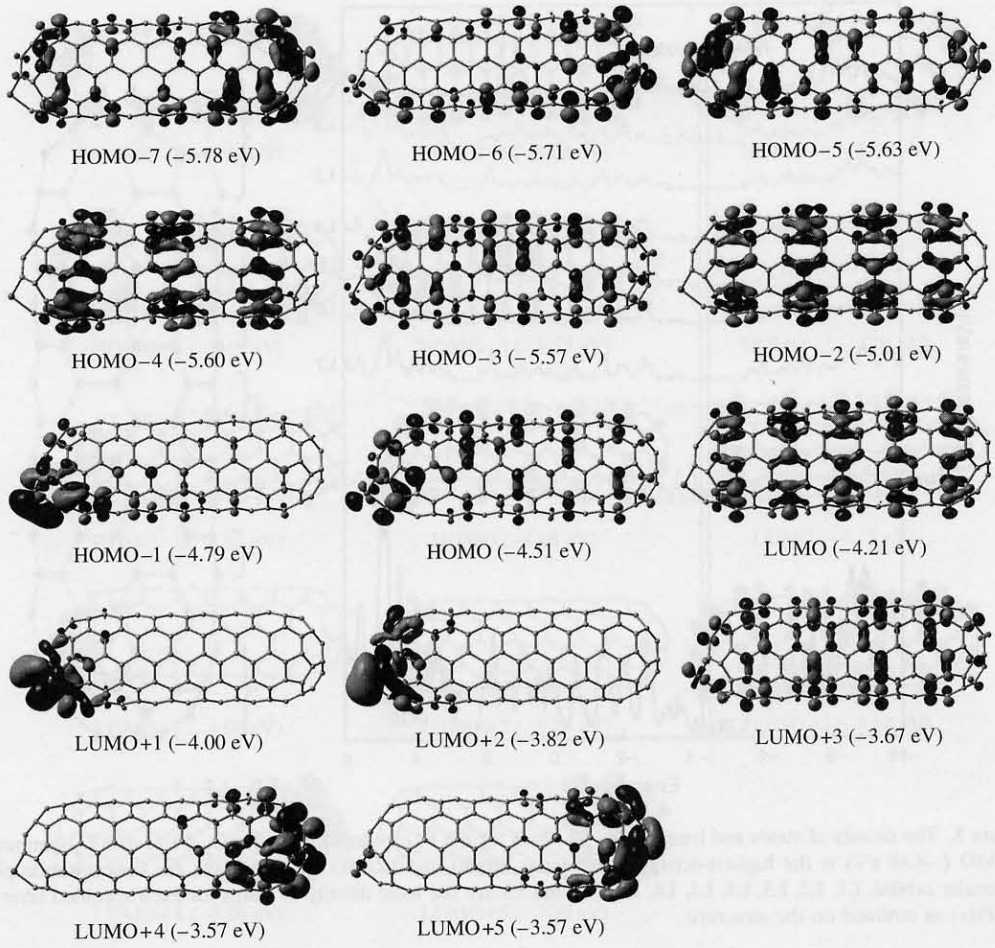

Figure 6. The frontier molecular orbitals of the Pt cap-end-doped nanorod $C_{169}Pt$(**ce**) with C_s symmetry. HOMO–n (p eV) is the nth orbital below the HOMO with orbital energy p eV. LUMO+m (q eV) is the mth orbital above the LUMO with orbital energy q eV.

the contribution to these two unoccupied MOs from the cap without doping diminishes. According to the MOs of $C_{169}Pt$(**ce**), one notices that the reactive center in $C_{169}Pt$(**ce**) is around the doping site of Pt. The Pt atom can donate electrons to electron acceptors and the empty 5*d* orbitals can accept electrons from electron donors, for example, in reaction with gases such CO, NH_3, and NO. NBO partial charge analysis indicates that Pt transfers about 0.80 (0.40 from 6*s* and 0.40 from 5*d*) electrons to the nearby carbon atoms: the electronic configuration of Pt is essentially [core]$5d^{8.60}6s^{0.60}$. The carbon atom connecting to Pt at the second layer from the doped cap end has the largest negative charge, −0.22.

3.3.2. $C_{169}Pt$(c)

The DOS and LDOS of each layer of $C_{169}Pt$(**c**) as shown in Fig. 7 are very similar to those in $C_{169}Pt$(**ce**). The structure of $C_{169}Pt$(**c**) is also similar to that of $C_{169}Pt$(**ce**), except for the doping regions around Pt. The Pt–C bond distance between Pt and the carbon atom in the top pentagon is 1.97 Å; the other two equivalent Pt–C bond distances are 2.00 Å. The long Pt–C bonds make the carbon atom of the top pentagon connected to Pt slightly point out of the pentagon as shown in Fig. 7. The FMOs of $C_{169}Pt$(**c**) as shown in Fig. 8 are very similar to those of $C_{169}Pt$(**ce**) in Fig. 6. The noticeable difference is that Pt contributes to the HOMO in $C_{169}Pt$(**c**) more than it does in $C_{169}Pt$(**ce**), which should enhance the reactivity of the Pt-doping site in $C_{169}Pt$(**c**). The electronic configuration of Pt is essentially [core]$5d^{8.63}6s^{0.60}$. The partial charge of Pt is 0.77 and the carbon atom connecting to Pt in the top pentagon has the largest negative partial charge, −0.25.

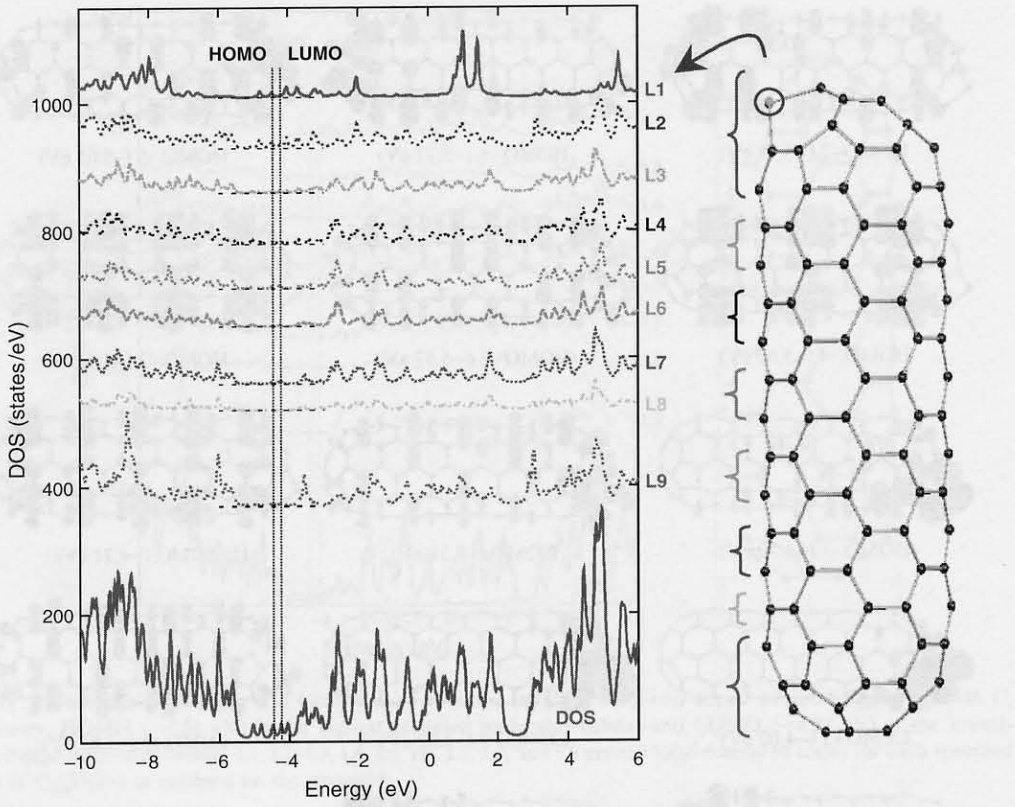

Figure 7. The density of states and local density of states for the Pt cap-doped nanorod $C_{169}Pt(\mathbf{c})$ with C_s symmetry. HOMO (−4.48 eV) is the highest-occupied molecular orbital and LUMO (−4.25 eV) is the lowest-unoccupied molecular orbital. L1, L2, L3, L4, L5, L6, L7, L8, and L9 are the local density of states for each specified layer of $C_{169}Pt(\mathbf{c})$ as outlined on the structure.

3.3.3. $C_{169}Pt(w)$

Figures 9 and 10 display the DOS, LDOS of each layer, and MOs for $C_{169}Pt(\mathbf{w})$. The DOS of $C_{169}Pt(\mathbf{w})$ around the FMO region is different from those of $C_{169}Pt(\mathbf{ce})$ and $C_{169}Pt(\mathbf{c})$. The contribution to the DOS of $C_{169}Pt(\mathbf{w})$ around the FMO region from Pt increases in comparison of those of $C_{169}Pt(\mathbf{ce})$ and $C_{169}Pt(\mathbf{c})$. The LDOS of Pt indicates that Pt makes significant contribution to the DOS at FMO region in $C_{169}Pt(\mathbf{w})$. The doping of Pt on the sidewall of the SWCNT also changes the LDOS of the neighboring carbon layers significantly, which is manifested by a comparison of the LDOS of L2 and L3 in Fig. 9 and those of L1 and L2 of C_{170} in Fig. 1. The LDOS contribution from each layer is also depicted by the FMOs shown in Fig. 10. From the HOMO–1 to the LUMO+3, Pt has significant contributions to each MO. The HOMO-LUMO gap (0.53 eV) of $C_{169}Pt(\mathbf{w})$ is larger than those of C_{170} (0.35 eV), $C_{169}Pt(\mathbf{ce})$ (0.30 eV), and $C_{169}Pt(\mathbf{c})$ (0.23 eV). In various chemical reactions, Pt will serve as catalytic centers, since it can accept and donate electrons. The electronic configuration of Pt is [core]$5d^{8.63}6s^{0.54}$. The partial charge of Pt is 0.83. The partial charge of the carbon atom connecting to Pt in the symmetric plane is −0.18, and this Pt–C bond distance is 2.01 Å. The partial charges of the other two equivalent carbon atoms connecting to Pt are −0.10, and these two equivalent Pt–C bond distances are 1.95 Å.

3.4. The SWCNT Segment $C_{200}H_{20}$

The other way to change the regioselectivity or reactivity of the SWCNT is creating active center through vacancy defects. The open-end SWCNTs and the end-capped SWCNTs with vacancy defects of the similar length can have very different electronic structures and reactivity. A (5,5) SWCNT segment with open ends is studied to understand such differences. The (5,5) SWCNT segment studied, $C_{200}H_{20}$, has 200 carbon atoms, saturated with 20 hydrogen atoms at the open ends, as shown in Fig. 11. The HOMO-LUMO gap of the

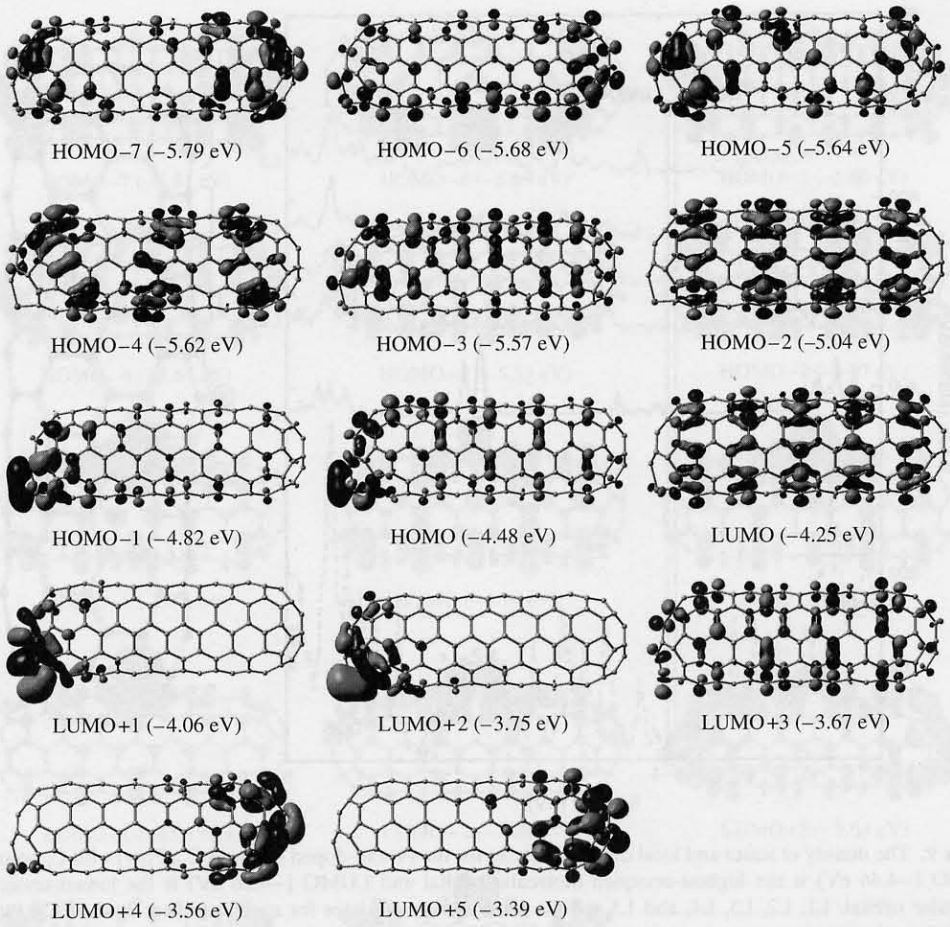

Figure 8. The frontier molecular orbitals of the Pt cap-doped nanorod $C_{169}Pt$(**c**) with C_s symmetry. HOMO–*n* (*p* eV) is the *n*th orbital below the HOMO with orbital energy *p* eV. LUMO+*m* (*q* eV) is the *m*th orbital above the LUMO with orbital energy *q* eV.

$C_{200}H_{20}$ segment (0.41 eV) is larger than those of the SWCNT rods, C_{170} (0.35 eV) and C_{180} (0.37 eV). Both of the HOMO and the LUMO are destabilized when compared with those of C_{170} and C_{180}, even though the $C_{200}H_{20}$ segment is longer than the SWCNT rods C_{170} and C_{180}. The stabilization effect of the hemispherical caps to the SWCNT rod is evident from the comparison of MO energies of the open-end SWCNT segments and SWCNT rods. The bands in the DOS of $C_{200}H_{20}$ as shown in Fig. 12 shift to higher-energy regions than those of the SWCNT rod C_{180} as shown in Fig. 2. The LDOS of the circular *cis*-polyene chains of $C_{200}H_{20}$ are very similar. Each layer contributes roughly equally to the FMOs, and there is no localized state on $C_{200}H_{20}$ as shown in Fig. 11. The HOMO and the LUMO of the short (5,5) SWCNT segments with open ends were studied before and showed alternating nodal pattern [3c], which is not observed here for the longer (5,5) SWCNT segments.

3.5. The Vacancy-Defected SWCNT Segment $C_{199}H_{20}$

Removing one carbon atom from the middle of the sidewall of $C_{200}H_{20}$ results in the vacancy-defected SWCNT $C_{199}H_{20}$ as shown in Fig. 13. The removal of one carbon atom from the SWCNT relaxes the geometric constrain in the curved sidewall of the SWCNT and stabilizes the HOMO and the LUMO, as indicated in Figs. 12 (for $C_{200}H_{20}$) and 14 (for $C_{199}H_{20}$). The HOMO-LUMO gap of $C_{199}H_{20}$ (0.39 eV) is slightly smaller than that of $C_{200}H_{20}$ (0.41 eV). The LDOS of different regions in $C_{200}H_{20}$ corresponding to the vacancy in $C_{199}H_{20}$ are plotted in Fig. 15 for better understanding the effect of creating vacancy defect to the electronic structure of the SWCNT. The contribution to the HOMO and the LUMO from the region of the vacancy defect in $C_{199}H_{20}$ (**L1** in Fig. 13) is much stronger than that of the

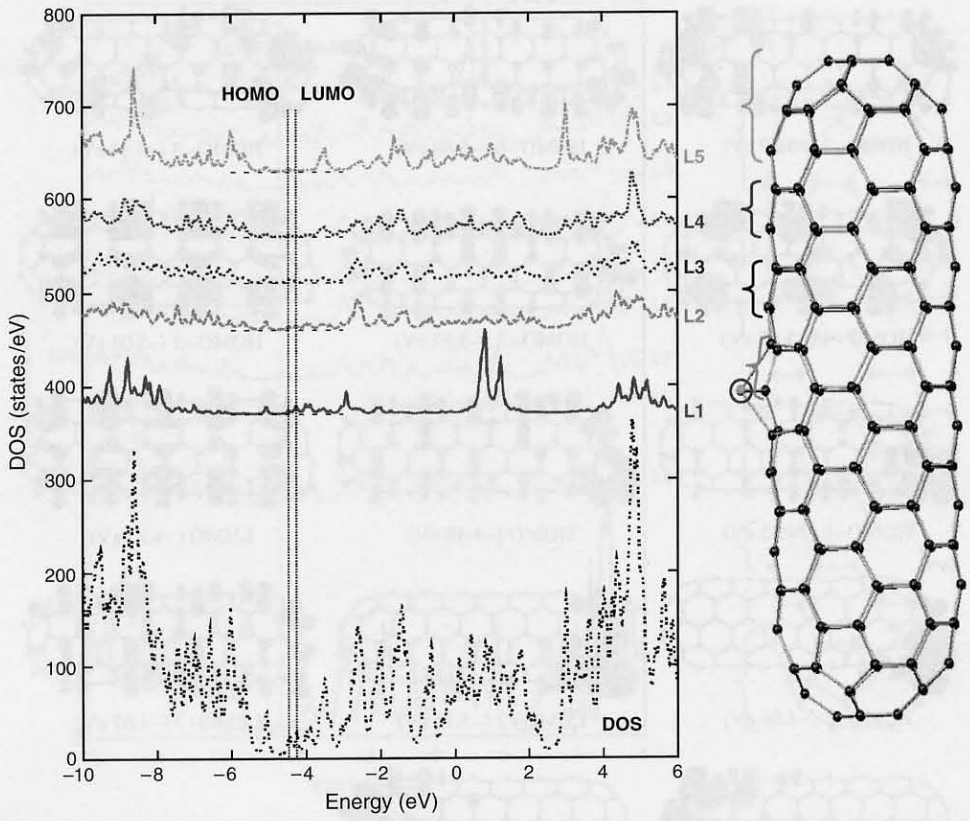

Figure 9. The density of states and local density of states for the Pt wall-doped nanorod $C_{169}Pt(\mathbf{w})$ with C_s symmetry. HOMO (−4.46 eV) is the highest-occupied molecular orbital and LUMO (−4.26 eV) is the lowest-unoccupied molecular orbital. L1, L2, L3, L4, and L5 are the local density of states for each specified layer of $C_{169}Pt(\mathbf{w})$ as outlined on the structure.

corresponding region in $C_{200}H_{20}$ (**L1** in Fig. 15). The FMOs of $C_{199}H_{20}$ in Fig. 14 reveal details of the contributions from different sites to the DOS of $C_{199}H_{20}$. The HOMO and the LUMO of $C_{199}H_{20}$ obviously have dominant contributions from the vacancy defect region. The π MOs in $C_{199}H_{20}$ is destructed to a large degree by the vacancy defect with respect to the MOs of $C_{200}H_{20}$ shown in Fig. 12. The vacancy defect region divides $C_{199}H_{20}$ into two parts at the middle nine-membered ring through the direction perpendicular to the SWCNT axis; this division is clearly manifested by the occupied MOs from the HOMO–3 to the HOMO, especially by the HOMO–2 and the HOMO–1. The HOMO consists of lone-pair electrons from the dangling carbon atom bonded only to two carbon atoms and the π bonds of the other carbon atoms of the nine-membered ring. The LUMO has dominant contributions from the nine-membered ring especially from the dangling carbon atom, but only half of the SWCNT contributes to the LUMO. The MOs of $C_{199}H_{20}$ indicate that the vacancy defect region will be the active center in chemical reactions.

4. CHEMICAL REACTION OF NO WITH THE VACANCY-DEFECTED SWCNT

4.1. Model Selection and Computational Details

The nine-membered ring at the vacancy defect region contributes significantly to the HOMO and the LUMO of $C_{199}H_{20}$ as shown in Fig. 16. The HOMO and the LUMO of $C_{199}H_{20}$ manifest that the vacancy defect region is an active site. According to the convention [18a], the vacancy defect as shown in Fig. 17 is called the 5-1DB (one pentagon and one dangling bond) defect. The dangling bond (DB) denotes that the carbon atom pointing out of the sidewall of $C_{199}H_{20}$ is directly bonded to only two neighboring carbon atoms and the unused

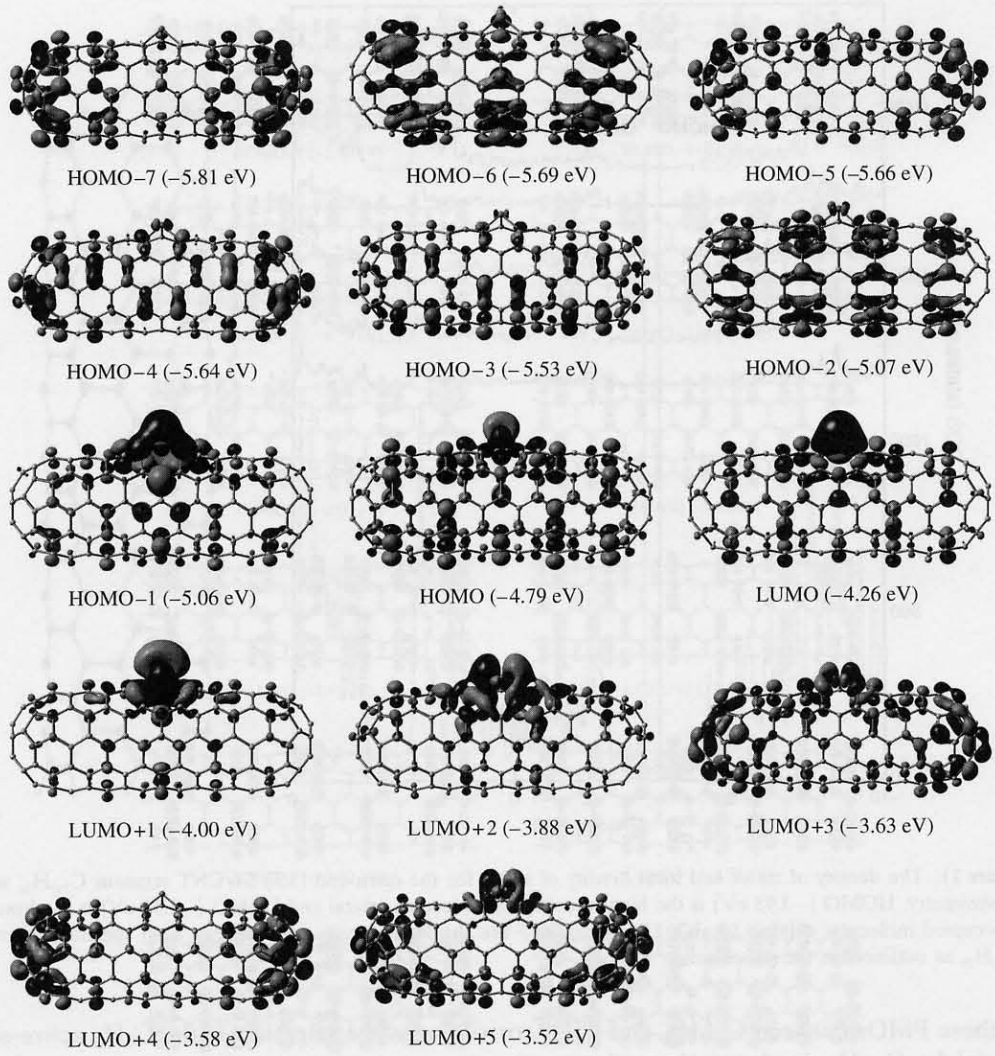

Figure 10. The frontier molecular orbitals of the Pt wall-doped nanorod $C_{169}Pt(\mathbf{w})$ with C_s symmetry. HOMO–n (p eV) is the nth orbital below the HOMO with orbital energy p eV. LUMO+m (q eV) is the mth orbital above the LUMO with orbital energy q eV.

sp^2 hybridized orbital on this carbon atom has a lone pair of electrons. This carbon atom directly bonded to only two neighboring carbon atoms is named as the dangling carbon atom.

In quantum chemical modeling of chemical reactions, fairly large set of basis functions is necessary for a good characterization of the potential energy surface (PES). However, because of the large size of the SWCNT clip, calculations with large basis sets are very time consuming. The relatively localized nature of the HOMO and the LUMO of $C_{199}H_{20}$ rationalizes the application of the ONIOM model [39] in the study of chemical reactions involving $C_{199}H_{20}$. Within the ONIOM model, to simulate the active vacancy defect site (the orange nine-membered ring in Fig. 17[a]), we use high-level theory to treat a model system C_9H_8 (as shown in Fig. 17[b]) whose hydrogens are the link atoms to replace the carbon atoms connected to the nine-membered ring. In the actual ONIOM model used in this work, the high-level theory is chosen to be the DFT method with the B3LYP [38, 53] exchange-correlation functional and the 6-31G(d) basis set whose good performances have been demonstrated in numerous chemical modeling before [54], and the low-level theory is based on the molecular mechanical description with the UFF force field [44] to capture the essential environmental effects exerted on the vacancy defect region by the surrounding carbon atoms. To validate this ONIOM model, we analyze the electronic structures of both $C_{199}H_{20}$ and C_9H_8 based on single-point DFT calculations at the B3LYP/6-31G level of theory. The HOMO and the LUMO of $C_{199}H_{20}$ and C_9H_8 are plotted in Fig. 16. The similarity

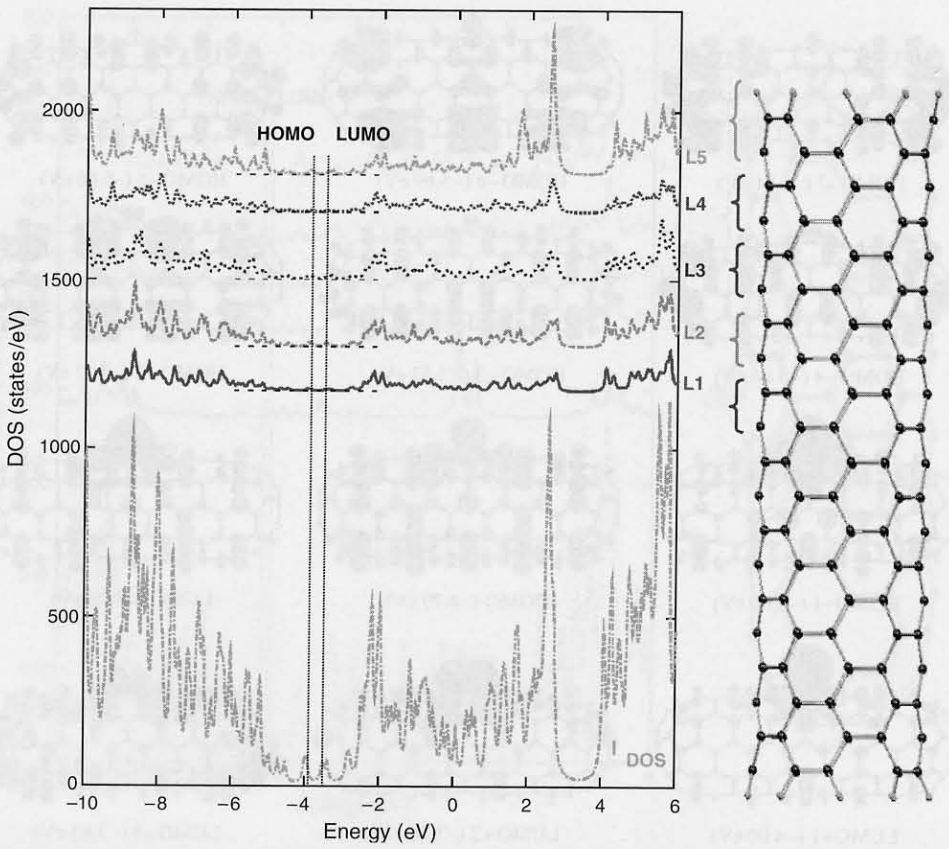

Figure 11. The density of states and local density of states for the open-end (5,5) SWCNT segment $C_{200}H_{20}$ with D_5 symmetry. HOMO (−3.93 eV) is the highest-occupied molecular orbital and LUMO (−3.52 eV) is the lowest-unoccupied molecular orbital. L1, L2, L3, L4, and L5 are the local density of states for each specified layer of $C_{200}H_{20}$ as outlined on the structure.

of these FMOs between $C_{199}H_{20}$ and C_9H_8 corroborates the selection of the C_9H_8 active-site model for $C_{199}H_{20}$ in chemical reactions.

All the stationary points on the PES are located with ONIOM(B3LYP/6-31G(d):UFF), and the nature of these stationary points are verified through computing the Hessians, the second-order derivative of the total energy with respect to the nuclear coordinates. A local minimum has all positive eigenvalues for the Hessian, and a transition state has one and only one negative eigenvalue. The connection of a transition state to two local minima along the intrinsic reaction coordinate is revealed by the eigenvector of the negative eigenvalue or the imaginary frequency in the vibrational analysis. Single-point calculations are performed at the B3LYP/6-31G level of theory based on the optimized geometry within the ONIOM model. The partial charge analysis is carried out with the NBO analysis [51]. In the following discussion, partial charge analysis and energetics are based on the B3LYP/6-31G single-point calculations.

4.2. Chemical Reaction of NO with the Vacancy-Defected SWCNT Segment $C_{199}H_{20}$

Partial charge analysis indicates that the dangling carbon atom has the largest positive charge and the oxygen atom in NO has a negative charge, as shown in Fig. 18. The specific conformation of the dangling carbon atom stretching out of the sidewall of the SWCNT facilitates the attack of NO to this carbon atom. Both of the partial charge and geometric structure of the 5-1DB defect and the partial charges on NO indicate that it is the oxygen atom in NO initially attacking the dangling carbon atom, C1, where the electrostatic attraction acts as the driving force for the initial reaction.

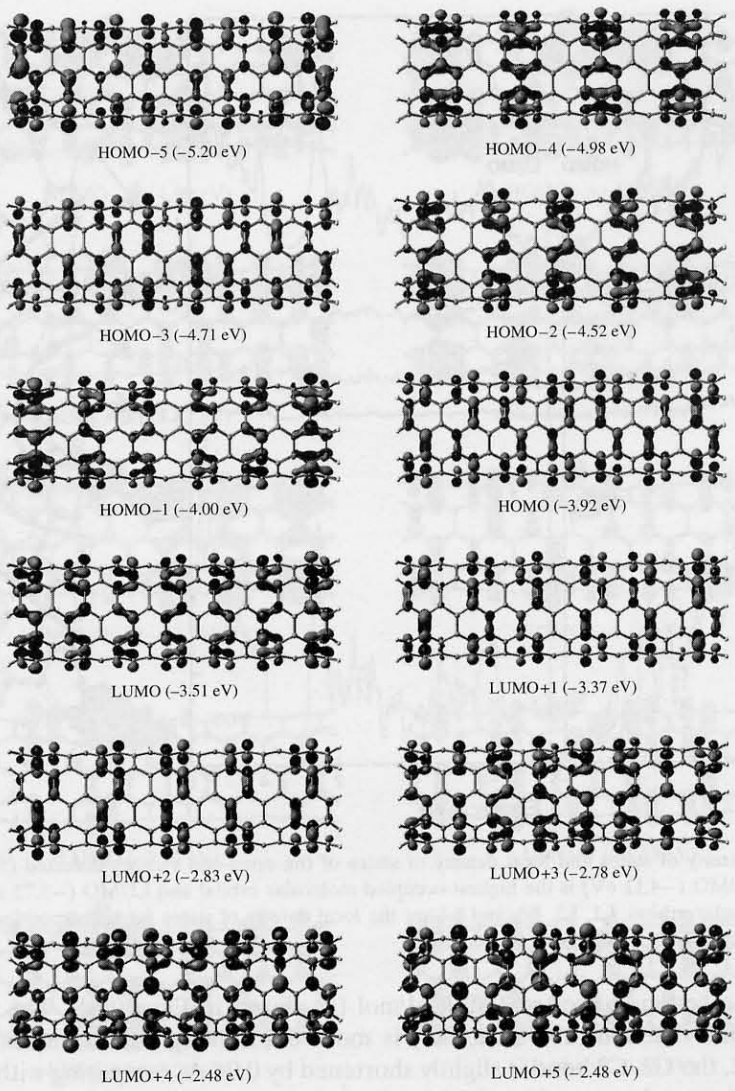

Figure 12. The frontier molecular orbitals of the open-end (5,5) SWCNT segment $C_{200}H_{20}$. HOMO–n (p eV) is the nth orbital below the HOMO with orbital energy p eV. LUMO+m (q eV) is the mth orbital above the LUMO with orbital energy q eV.

Indeed, we locate the initial transition state (TS1) with O of NO attacking the dangling carbon atom, C1, as shown in Fig. 18(c). In TS1, the C1–O bond distance is 1.70 Å. The imaginary vibrational mode clearly indicates the attacking of O to C1. The bond distances of NO and the 5-1DB ring are slightly elongated in TS1. The initial NO-attacking reaction is quite feasible because its barrier is only 8.6 kcal/mol. Such a mild reaction barrier is mainly due to the electrostatic attraction in TS1 and the strong MO overlaps between O and C1 in the HOMO–7, the HOMO–18, and the HOMO–19 as shown in Fig. 18.

After overcoming the initial reaction barrier, the system reaches the first intermediate, LM1, in which NO forms a bridge connecting C1 and C2, as shown in Fig. 19(a). In LM1, the most noticeable geometric change is the elongation of the C2–C3 bond. Comparing to the short bond distance of 1.55 Å in TS1, the C2–C3 bond distance gets longer in LM1, becoming 1.69 Å and nearly reaching the broken limit of a single CC bond. LM1 is 19.1 kcal/mol more stable than the reactants, thus the initial reaction is exothermic. The release of the heat of formation of the initial reaction facilitates the consequent reaction step after forming LM1, when the loose C2–C3 bond exposes itself as the reactive center in the newly formed NO-(5-1DB) eight-membered ring, which is flexible enough to allow some distortions.

The next step is the tautomerization of LM1 occurring at the C2–C3 region and the N atom begins to form a bond with C3, as the system reaches the transition state, TS2, after

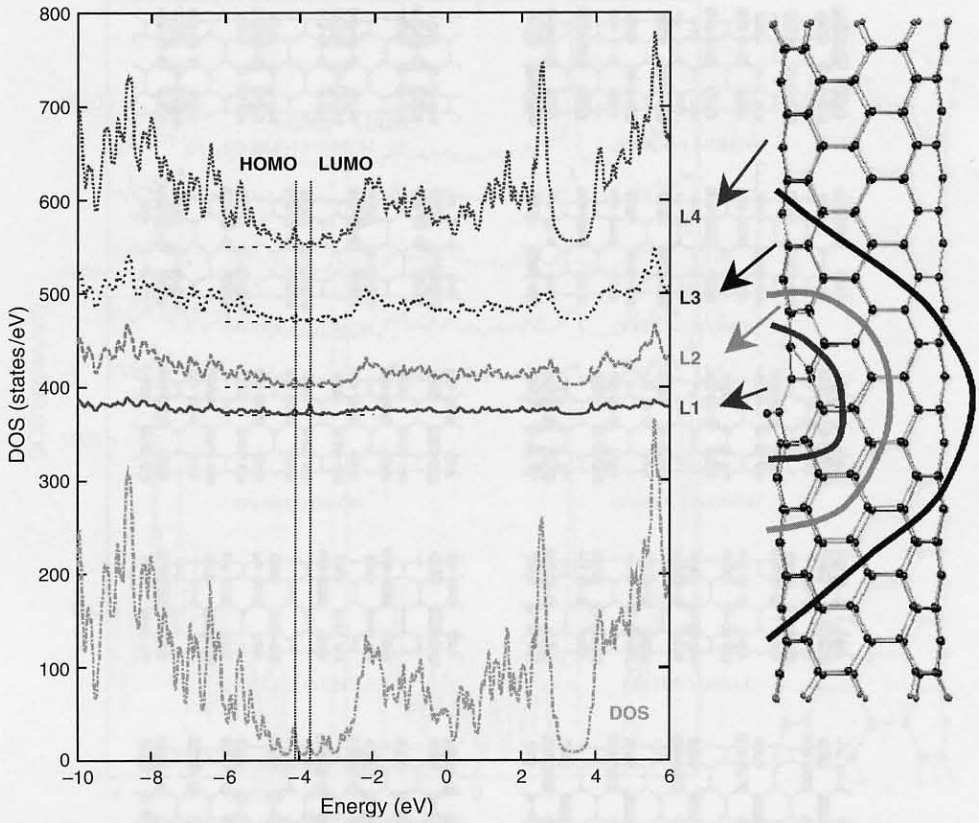

Figure 13. The density of states and local density of states of the open-end vacancy-defected (5,5) SWCNT segment $C_{199}H_{20}$. HOMO (−4.11 eV) is the highest-occupied molecular orbital and LUMO (−3.72 eV) is the lowest-unoccupied molecular orbital. L1, L2, L3, and L4 are the local density of states for each specified group of atoms of $C_{199}H_{20}$ as outlined on the structure.

overcoming a reaction barrier of 12.2 kcal/mol (as shown in Fig. 19[b]). The heat released during the initial reaction (19.1 kcal/mol) is more than enough to surmount this reaction barrier. In TS2, the C2–C3 bond is slightly shortened by 0.04 Å, comparing with the structure of LM1. The distance between N and C3 is 1.94 Å, indicating a N–C3 bond formation motion at TS2. After breaking the C2–C3 bond, the system reaches the second intermediate, LM2, as shown in Fig. 19(c).

In LM2, N simultaneously bonds to C2 and C3 with bond distances 1.39 Å and 1.40 Å, respectively. The distance between C2 and C3 in LM2 is 2.39 Å, which clearly indicates no strong bonding between C2 and C3. The formation of LM2 is highly exothermic. The system releases 85.5 kcal/mol energy descending from TS2. This large amount of energy release enables the system to undergo further reaction steps even to break strong covalent bonds. When N substitutes O on C1, the system reaches the third transition state, TS3, located 41.1 kcal/mol above LM2 (as shown in Fig. 19[d]).

In TS3, the distances between O and C1 and between N and C1 are 1.98 Å and 2.14 Å, respectively. This structure of TS3 clearly indicates that it connects two intermediates with either O or N bonded to C1. One of these two intermediate is LM2 with O bonded to C1, and the other intermediate is LM3 with N bonded to C1 (as shown in Fig. 19[e]). In LM3, the N atom concurrently bonds to C1, C2, C3, and O, filling in the original vacancy defect. According to the relative energies of these stationary points, the reaction from LM2 to LM3 is thermodynamically highly facile.

Overall, when $C_{199}H_{20}$ reacts with NO, NO attacks the dangling carbon atom of the 5-1DB defect. After going over a small reaction barrier, the system reaches an intermediate (LM1) with NO bridging across C1 and C2 in the 5-1DB ring and releases about 19.1 kcal/mol of energy. Following the insertion of N into the C2–C3 bond of the 5-1DB ring, the system undergoes a pseudo-SN2 reaction, in which the N atom replaces the O atom bonded to

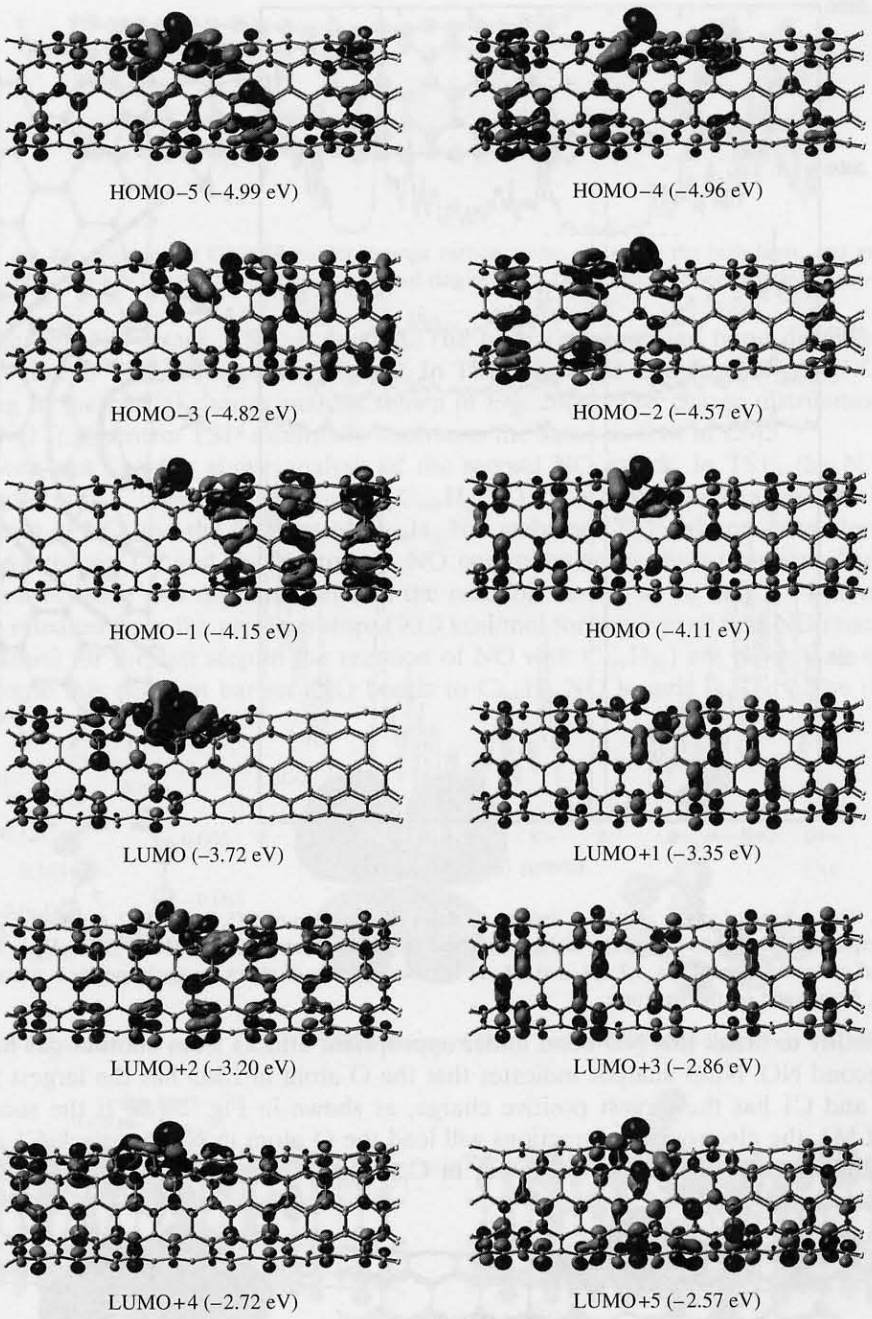

Figure 14. The frontier molecular orbitals of the open-end vacancy-defected (5,5) SWCNT segment $C_{199}H_{20}$. HOMO–n (p eV) is the nth orbital below the HOMO with orbital energy p eV. LUMO+m (q eV) is the mth orbital above the LUMO with orbital energy q eV.

C1 and the O atom flips up, pointing outwards from the sidewall of the nanotube. The net reaction is the insertion of the N end of NO into the vacancy defect with the initial attack of the O end of NO to the dangling carbon atom. This reaction is highly exothermic with a net energy release of 90.0 kcal/mol, indicating that the repairing of vacancy-defected SWCNT with NO is thermodynamically and kinetically feasible.

4.3. Chemical Reaction of NO with $C_{199}H_{20}NO$

According to the structure of LM3, N bonds to the four atoms C1, C2, C3, and O with single-bond distances. The unpaired electron mainly stays on the O atom, which makes LM3 reactive for further reactions with NO. The elongated NO bond distance in LM3 reveals

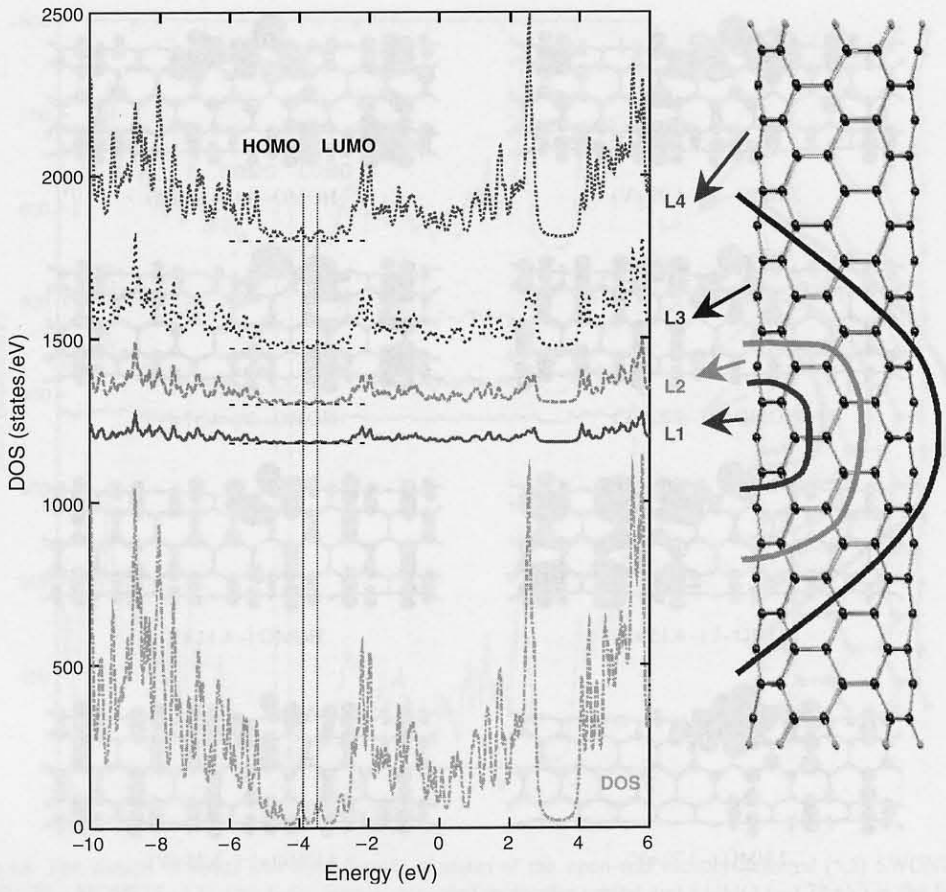

Figure 15. The density of states and local density of states of the open-end (5,5) SWCNT segment $C_{200}H_{20}$ with D_5 symmetry. HOMO (−3.93 eV) is the highest-occupied molecular orbital and LUMO (−3.52 eV) is the lowest-unoccupied molecular orbital. L1, L2, L3, and L4 are the local density of states for each specified group of atoms of $C_{200}H_{20}$ as outlined on the structure.

the feasibility to break this NO bond under appropriate attacks from another gas molecule, *e.g.*, a second NO. NBO analysis indicates that the O atom in LM3 has the largest negative charges and C1 has the largest positive charge, as shown in Fig. 20(a). If the second NO attacks LM3, the electrostatic attractions will lead the O atom in NO to attack C1 and lead the N atom in NO to attack the O atom in $C_{199}H_{20}NO$. Accordingly, the transition state

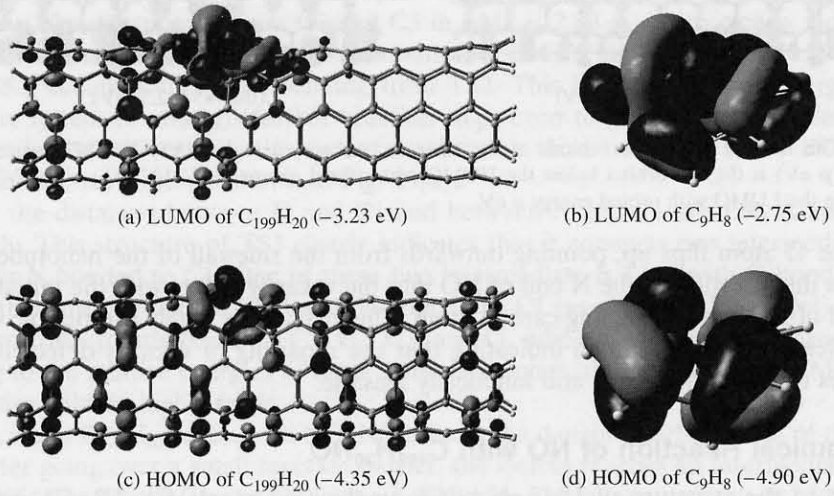

(a) LUMO of $C_{199}H_{20}$ (−3.23 eV)

(b) LUMO of C_9H_8 (−2.75 eV)

(c) HOMO of $C_{199}H_{20}$ (−4.35 eV)

(d) HOMO of C_9H_8 (−4.90 eV)

Figure 16. The highest-occupied molecular orbital (HOMO) and the lowest-unoccupied molecular orbital (LUMO) of $C_{199}H_{20}$ and C_9H_8.

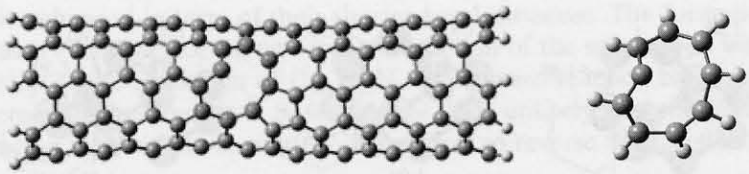

(a) (b)

Figure 17. (a) The two-layered ONIOM model (orange carbon atoms are set as the high layer, and grey carbon atoms are set as the low layer); (b) the nine-membered ring of the 5-1DB defect capped with hydrogen atoms.

for the second NO attack, TS1′, is located. The partial charges and bond distances of the 5-1DB region in TS1′ are shown in Fig. 20. In TS1′, electrons flow from $C_{199}H_{20}NO$ to NO according to the partial charge analysis shown in Fig. 20(b). The charge distribution of the $C_{199}H_{20}NO$ fragment in TS1′ essentially maintains the same as that in LM3.

However, not like the above analysis of the second NO attack, in TS1′, the N atom in NO attacks both C1 and the O atom of $C_{199}H_{20}NO$. The electrostatic attraction between the N atom in NO and the O atom of $C_{199}H_{20}NO$ stabilizes TS1′, whereas the electrostatic repulsion between C1 and the N atom in NO counterbalances this attraction. The overall interaction of these two reactants renders the reaction barrier to be only 3.7 kcal/mol. The energies released from the previous steps (90.0 kcal/mol for the overall first-NO reaction and 38.7 kcal/mol for the last step in the reaction of NO with $C_{199}H_{20}$) are more than sufficient to overcome this reaction barrier. NO bonds to $C_{199}H_{20}NO$ loosely in TS1′. The distances

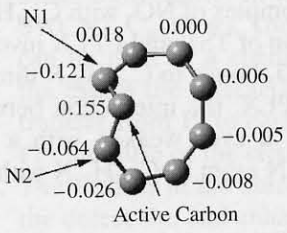

(a) NBO charges in $C_{199}H_{20}$

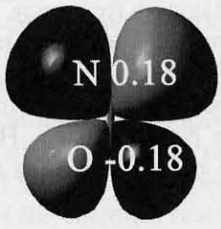

(b) NBO charges of NO

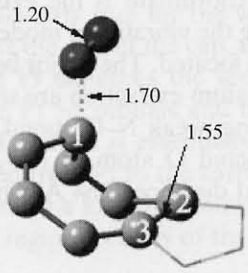

(c) relevant bond distances in **TS1** ($\Delta E = 8.6$)

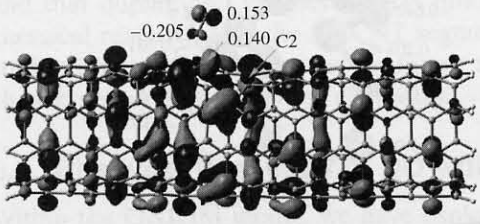

(f) HOMO of **TS1** (−4.66 eV) and NBO charges

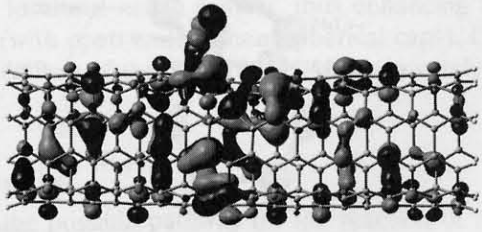

(g) HOMO−7 of **TS1** (−5.86 eV)

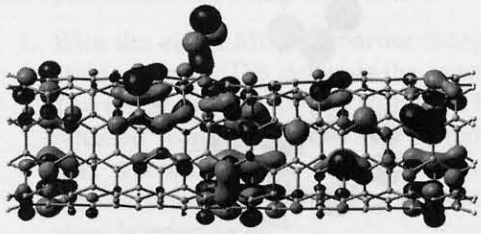

(h) HOMO−18 of **TS1** (−6.49 eV)

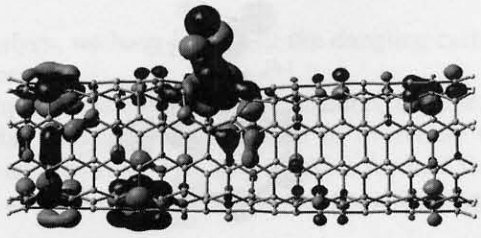

(i) HOMO−19 of **TS1** (−6.54 eV)

Figure 18. Partial charges of $C_{199}H_{20}$ and NO, bond distances (in Å) of the 5-1DB defect region of the initial transition state, **TS1**, for NO reacting with $C_{199}H_{20}$. Relative energy (in kcal/mol) of **TS1** with respect to NO and $C_{199}H_{20}$ from DFT calculations at the B3LYP/6-31G level of theory and the frontier molecular orbitals relevant to the interaction between NO and $C_{199}H_{20}$.

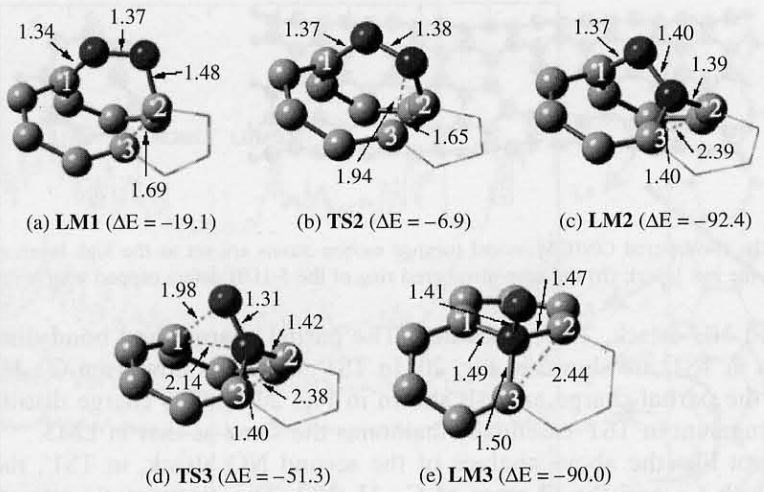

Figure 19. The relevant bond distances (in Å) of the 5-1DB defect region in the stationary points, LM1, TS2, LM3, TS3, and LM3 along the reaction of NO with $C_{199}H_{20}$, and their relative energies (in kcal/mol) with respect to NO and $C_{199}H_{20}$ from DFT calculations at the B3LYP/6-31G level of theory.

between the N atom in NO and the O atom of $C_{199}H_{20}NO$ and between the N atom in NO and C1 of $C_{199}H_{20}NO$ is 2.55 Å and 1.61 Å, respectively.

According to the imaginary vibrational mode of TS1′, the major motion along the intrinsic reaction coordinate is the extraction of the O atom from $C_{199}H_{20}NO$ by the second NO. Following the vibrational mode of the imaginary frequency, a complex of NO_2 with $C_{199}H_{20}N$, CPLX, is located. The major bond distances of the 5-1DB region of TS1′ and CPLX involved in the O-atom extraction are shown in Fig. 20(d). In CPLX, NO_2 bonds to $C_{199}H_{20}N$ through a very long, weak N–C1 bond with bond length 1.64 Å. In CPLX, the interaction between the extracted O atom of NO_2 with the N atom in $C_{199}H_{20}N$ is even weaker, with a very long bond distance, 2.64 Å, whereas the bonding between the N atom in $C_{199}H_{20}N$ with C1,

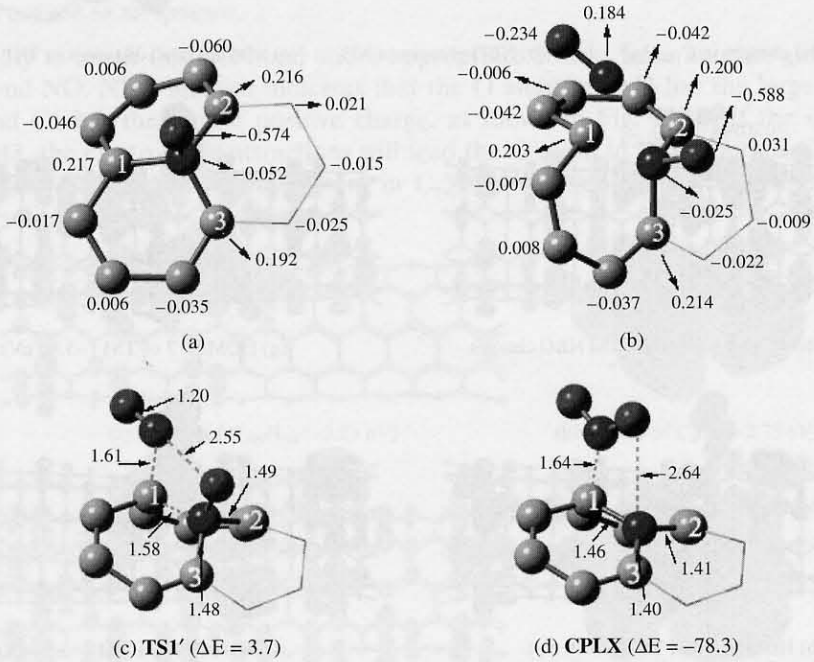

Figure 20. Partial charges of the 5-1DB defect region in LM3 and in the transition state, TS1′, for the second NO reacting with $C_{199}H_{20}NO$, bond distances (in Å) of the 5-1DB defect region of TS1′ and the corresponding product, CPLX, and relative energies (in kcal/mol) of TS1′ and CPLX with respect to the sum of the energies of NO and $C_{199}H_{20}NO$ from DFT calculations at the B3LYP/6-31G level of theory.

C2, and C3 is enhanced in term of their shorter bond distances. The formation of the final product releases 78.3 kcal/mol energy from the reaction of the second NO with $C_{199}H_{20}NO$. In the final step of the formation of $C_{199}H_{20}N$, the forward reaction barrier is 3.7 kcal/mol and the reverse reaction barrier is 82.0 kcal/mol. It is unlikely that the final complex will climb over such a big reaction barrier (82.0 kcal/mol) to reverse the reaction.

5. CONCLUDING REMARKS

5.1. The Pt-Doped SWCNT Rods and Vacancy-Defected SWCNT Segments

Within DFT, the electronic structures and chemical reactivities of the SWCNT rods C_{170} and C_{180}, the Pt-doped SWCNT rods $C_{169}Pt(ce)$, $C_{169}Pt(c)$, and $C_{169}Pt(w)$, and the (5,5) SWCNT segments with open ends and vacancy defect have been studied in detail. According to the analysis, we have reached the following conclusions:

1. The hemispherical caps stabilize the SWCNT rods and the SWCNT rods have smaller HOMO-LUMO gaps than those of the SWCNT segments with open ends. Indeed localized states exist on the hemispherical caps in the SWCNT rods, as confirmed by the DOS, the LDOS, and the FMOs. The circular *cis*-polyene chain between the cap and the sidewall of the SWCNT is active in chemical reactions according to the MO analysis.
2. The ground state of the Pt-doped SWCNT rod is singlet.
3. The doping of Pt in the SWCNT rod results in localized states at Pt, thus rendering Pt as an active center in chemical reactions, which is particularly true for the wall-doped SWCNT, $C_{169}Pt(w)$. The Pt-doped SWCNT rod with Pt at the end of the cap, $C_{169}Pt(ce)$, can be used as a chemical sensor, since the doping of Pt enhances the sensitivity of the cap in the interaction with the substrate due to the Pt $5d$ orbitals and the charge transfer from Pt to carbon atoms. In Pt-doped SWCNT rod, Pt is essentially acting as Pt^+, because of the charge transfer of about one electron from Pt to the carbon atoms.
4. The vacancy in the defected SWCNT with open ends creates a localized active center at the defect site and enhances the chemical reactivity and regioselectivity of the open-end defected SWCNT.

Present DFT studies reveal that the hemispherical caps stabilize the SWCNT segments and that doping and vacancy defects produce localized active centers, thus enhancing the chemical reactivities of the SWCNT segments (with open ends or hemispherical caps). Our studies point to new directions for future applications of the SWCNT segments in catalysis, chemic sensor, and nanotube chemistry.

5.2. Chemical Reactions of NO with $C_{199}H_{20}$

Within the ONIOM model, we have explored the possible pathway for the reaction of NO with the vacancy-defected SWCNT segment $C_{199}H_{20}$, analyzed the energetics of the reaction and reached the following conclusions:

1. With the aid of MO and partial charge analysis, we have identified the dangling carbon atom in the 5-1DB defect is the reactive center.
2. The initial reaction of NO with $C_{199}H_{20}$ is quite feasible. Along the reaction, the energy released from a previous step is more than enough for the system to overcome the next reaction barrier: the reaction is self-accelerating. The first product formed from the reaction of NO with $C_{199}H_{20}$ is stable and reactive because of the dangling oxygen atom bonded to N.
3. When the second NO reacts with $C_{199}H_{20}NO$, NO extracts the O atom bonded to N in $C_{199}H_{20}NO$, thus forming a NO_2-$C_{199}H_{20}N$ complex. The energy released from the reaction of the first NO with $C_{199}H_{20}$ is sufficient for the reaction of the second NO with $C_{199}H_{20}NO$ to overcome its reaction barrier. This reaction of the second NO with $C_{199}H_{20}NO$ is also highly exothermic.

In summary, with DFT, we have studied the geometric and electronic structures of the SWCNT nanorods and segments, the Pt-dope SWCNT nanorods, the vacancy-defected SWCNT segment, and the reactions of NOs with the vacancy-defected SWNCT segment $C_{199}H_{20}$. We have found that the doping of Pt in the SWCNT rods enhances the reactivity of the SWCNT rods and suggest a new way to fabricate chemical sensors. The vacancy site of the vacancy-defected SWCNT segment is an active center. The reaction of NOs with $C_{199}H_{20}$ is quite feasible. The N end of the first NO inserts into the 5-1DB defect site; the second NO extracts the O atom bonded to N in $C_{199}H_{20}NO$. These reactions are thermally self-catalyzed reaction. The new reaction mechanism provides a novel way to repair the damaged SWCNTs and introduces a new method to fabricate the heteroatom-doped SWCNT at specific site under mild conditions. We believe that our theoretical investigation provides a necessary guidance for the future SWCNT functionalization.

ACKNOWLEDGMENTS

The financial support from the Natural Sciences and Engineering Research Council of Canada is gratefully acknowledged. L. V. L. received the Gladys Estella Laird Fellowship and the Charles A. McDowell Fellowship from the Department of Chemistry at the University of British Columbia. W. Q. T. received a postdoctoral fellowship from the Japan Society for the Promotion of Science and thanks to Professor Yuriko Aoki at Kyushu University for her hospitality.

REFERENCES

1. (a) S. Iijima and T. Ichihashi, *Nature (London)* 363, 603 (1993); (b) D. S. Bethune, C. H. Kiang, M. S. de Vries, G. Gorman, R. Savoy, J. Vazquez, and R. Beyers, *Nature (London)* 363, 605 (1993).
2. (a) S. Niyogi, M. A. Hamon, H. Hu, B. Zhao, P. Bhowmik, R. Sen, M. E. Itkis, and R. C. Haddon, *Acc. Chem. Res.* 35, 1105 (2002); (b) T. Hermraj-Benny, S. Banerjee, and S. S. Wong, *Chem. Mater.* 16, 1855 (2004); (c) J.-M. Nhut, P. Nguyen, C. Pham-Huu, N. Keller, and M.-J. Ledoux, *Catal. Today* 91, 91 (2004); (d) J. Zhang, H. Zou, Q. Qing, Y. Yang, Q. Li, Z. Liu, X. Guo, and Z. Du, *J. Phys. Chem. B* 107, 3712 (2003).
3. (a) T. Yamabe, M. Imade, M. Tanaka, and T. Sato, *Synth. Metals* 117, 61 (2001); (b) X. Lu, F. Tian, Y. Feng, X. Xu, N. Wang, and Q. Zhang, *Nano Lett.* 2, 1325 (2002); (c) J. Li, Y. Zhang, and M. Zhang, *Chem. Phys. Lett.* 364, 328 (2002); (d) J. Cioslowski, N. Rao, and D. Moncrieff, *J. Am. Chem. Soc.* 124, 8485 (2002); (e) T. Kar, B. Akdim, X. Duan, and R. Pachter, *Chem. Phys. Lett.* 392, 176 (2004); (f) M. Zhao, Y. Xia, J. P. Lewis, and L. Mei, *J. Phys. Chem. B* 108, 9599 (2004); (g) S. Gustavsson, A. Rosén, H. Grennberg, and K. Bolton, *Chem. Eur. J.* 10, 2223 (2004); (h) E. Joselevich, *Chem. Phys. Chem.* 5, 619 (2004); (i) Z. Zhou, M. Steigerwald, M. Hybertsen, L. Brus, and R. Friesner, *J. Am. Chem. Soc.* 126, 3597 (2004); (j) T. Yumura, K. Hirahara, S. Bandow, K. Yoshizawa, and S. Iijima, *Chem. Phys. Lett.* 386, 38 (2004).
4. (a) D. L. Carroll, P. Redlich, P. M. Ajayan, J. C. Charlier, X. Blase, A. De Vita, and R. Car, *Phys. Rev. Lett.* 78, 2811 (1997); (b) Z. Klusek, P. Kowalczyk, and P. Byszewski, *Vacuum* 63, 145 (2001); (c) M. Shiraishi and M. Ata, *Synth. Metals* 128, 235 (2002); (d) K. A. Dean and B. R. Chalamala, *J. Vac. Sci. Technol. B* 21, 868 (2003); (e) H. Kim, J. Lee, S.-J. Kahng, Y.-W. Son, S. B. Lee, C.-K. Lee, J. Ihm, and Y. Kuk, *Phys. Rev. Lett.* 90, 216107 (2003).
5. (a) X. Blase, L. X. Benedict, E. L. Shirley, and S. G. Louie, *Phys. Rev. Lett.* 72, 1878 (1994); (b) Y. H. Lee, S. G. Kim, and D. Tománek, *Phys. Rev. Lett.* 78, 2393 (1997); (c) T. Yaguchi and T. Ando, *J. Phys. Soc. Jpn.* 70, 1327 (2001); (d) T. Yaguchi and T. Ando, *J. Phys. Soc. Jpn.* 71, 2224 (2002); (e) J. Jiang, J. Dong, and D. Y. Xing, *Phys. Rev. B* 65, 245418 (2002); (f) S. Compernolle, L. Chibotaru, and A. Ceulemans, *J. Chem. Phys.* 119, 2854 (2003); (g) L. Chico and W. Jaskólski, *Phys. Rev. B* 69, 085406 (2004); (h) G. Y. Guo, K. C. Chu, D.-S. Wang, and C.-G. Duan, *Phys. Rev. B* 69, 205416 (2004).
6. P. M. Ajayan and O. Z. Zhou, in "Carbon Nanotubes Synthesis, Structure, Properties, and Applications" (M. S. Dresselhaus, G. Dresselhaus, and P. Avoutis, Eds.). Springer-Verlag, Berlin, 2001.
7. (a) P. Avouris, *Acc. Chem. Res.* 35, 1026 (2002); (b) R. D. Antonov and A. T. Johnson, *Phys. Rev. Lett.* 83, 3274 (1999); (c) M. S. Fuhrer, J. Nygård, L. Shih, M. Forero, Y.-G. Yoon, M. S. C. Mazzoni, H. J. Choi, J. Ihm, S. G. Louie, A. Zettl, and P. L. McEuen, *Science* 288, 494 (2000).
8. (a) J. Kong, N. R. Franklin, C. Zhou, M. G. Chapline, S. Peng, K. Cho, and H. Dai, *Science* 287, 622 (2000); (b) P. G. Collins, K. Bradley, M. Ishigami, and A. Zettl, *Science* 287, 1801 (2000); (c) A. Goldoni, R. Larciprete, L. Petaccia, and S. Lizzit, *J. Am. Soc. Chem.* 125, 11329 (2003).
9. O. Zhou, H. Shimoda, B. Gao, S. Oh, L. Fleming, and G. Yue, *Acc. Chem. Res.* 35, 1045 (2002).
10. W. B. Choi, D. S. Chung, J. H. Kang, H. Y. Kim, Y. W. Jin, I. T. Han, Y. H. Lee, J. E. Jung, N. S. Lee, G. S. Park, and J. M. Kim, *Appl. Phys. Lett.* 75, 3129 (1999).
11. P. Serp, M. Corrias, and P. Kalck, *Appl. Catal. A* 253, 337 (2003).

12. (a) S. Botti, R. Ciardi, L. De Dominicis, L. S. Asilyan, R. Fantoni, and T. Marolo, *Chem. Phys. Lett.* 378, 117 (2003); (b) S. Tatsuura, M. Furuki, Y. Sato, I. Iwasa, M. Tian, and H. Mitsu, *Adv. Mater.* 15, 534 (2003). (c) S. Y. Set, H. Yaguchi, Y. Tanaka, and M. Jablonski, *J. Lightwave Technol.* 22, 51 (2004); (d) A. G. Rozhin, Y. Sakakibara, M. Tokumoto, H. Kataura, and Y. Achiba, *Thin Solid Films* 464, 368 (2004).
13. (a) N. Hamada, S.-I. Sawada, and A. Oshiyama, *Phys. Rev. Lett.* 68, 1579 (1992); (b) M. S. Dresselhaus, G. Dresselhaus, and P. C. Eklund, "Science of Fullerenes and Carbon Nanotubes," Chap. 19, Academic, San Diego, 1995.
14. I. W. Chiang, B. E. Brinson, A. Y. Huang, P. A. Willis, M. J. Bronikowski, J. L. Margrave, R. E. Smalley, and R. H. Hauge, *J. Phys. Chem. B* 105, 8297 (2001).
15. (a) E. T. Mickelson, C. B. Huffman, A. G. Rinzler, R. E. Smalley, R. H. Hauge, and J. L. Margrave, *Chem. Phys. Lett.* 296, 188 (1998); (b) P. J. Boul, J. Liu, E. T. Mickelson, C. B. Huffman, L. M. Ericson, I. W. Chiang, K. A. Smith, D. T. Colbert, R. H. Hauge, J. L. Margrave, and R. E. Smalley, *Chem. Phys. Lett.* 310, 367 (1999); (c) M. Holzinger, O. Vostrowsky, F. H. Hirsch, F. Hennrich, M. Kappes, R. Weiss, and F. Jellen, *Angew. Chem. Int. Ed.* 40, 4002 (2001); (d) J. L. Bahr and J. M. Tour, *Chem. Mater.* 13, 3823 (2001); (e) J. L. Bahr, J. Yang, D. V. Kosynkin, M. J. Bronikowski, R. E. Smalley, and J. M. Tour, *J. Am. Chem. Soc.* 123, 6536 (2001); (f) V. Georgakilas, K. Kordatos, M. Prato, D. M. Guldi, M. Holzinger, and A. Hirsch, *J. Am. Chem. Soc.* 124, 760 (2002); (g) P. Umek, J. W. Seo, K. Hernadi, A. Mrzel, P. Pechy, D. D. Mihailovic, and L. Forr, *Chem. Mater.* 15, 4751 (2003); (h) J. L. Stevens, A. Y. Huang, H. Peng, L. W. Chiang, V. N. Khabashesku, and J. L. Margrave, *Nano Lett.* 3, 331 (2003); (i) H. Peng, L. B. Alemany, J. L. Margrave, and V. N. Khabashesku, *J. Am. Chem. Soc.* 125, 15174 (2003); (j) H. Hu, B. Zhao, M. A. Hamon, K. Kamaras, M. E. Itkis, and R. C. Haddon, *J. Am. Chem. Soc.* 125, 14893 (2003); (k) S. Banerjee, M. G. C. Kahn, and S. S. Wong, *Chem. Eur. J.* 9, 1898 (2003); (l) B. Zhao, H. Hu, and R. C. Haddon, *Adv. Funct. Mater.* 14, 71 (2004); (m) L. Zhang, V. U. Kiny, H. Peng, J. Zhu, R. F. M. Lobo, J. L. Margrave, and V. N. Khabashesku, *Chem. Mater.* 16, 2055 (2004).
16. M. A. Hamon, J. Chen, H. Hu, Y. Chen, M. E. Itkis, A. M. Rao, P. C. Eklund, and R. C. Haddon, *Adv. Mater.* 11, 834 (1999).
17. J. L. Bahr and J. M. Tour, *J. Mater. Chem.* 12, 1952 (2002).
18. (a) P. M. Ajayan, V. Ravikumar, and J.-C. Charlier, *Phys. Rev. Lett.* 81, 1437 (1998). (b) M. Igami, T. Nakanishi, and T. Ando, *J. Phys. Soc. Jpn.* 68, 716 (1999); (c) M. Igami, T. Nakanishi, and T. Ando, *Physica B* 284, 1746 (2000); (d) A. V. Krasheninnikov and K. Nordlund, *Phys. Solid State* 44, 470 (2002); (e) J.-C. Charlier, *Acc. Chem. Res.* 35, 1063 (2002); (f) A. V. Krasheninnikov and K. Nordlund, *J. Vac. Sci. Technol. B* 20, 728 (2002); (g) A. J. Lu and B. C. Pan, *Phys. Rev. Lett.* 92, 105504 (2004); (f) V. V. Belavin, L. G. Bulusheva, and A. V. Okotrub, *Int. J. Quantum Chem.* 96, 239 (2004); (g) L. Valentini, F. Mercuri, I. Armentano, C. Cantalini, S. Picozzi, L. Lozzi, S. Santucci, A. Sgamellotti, and J. M. Kenny, *Chem. Phys. Lett.* 387, 356 (2004).
19. (a) D. L. Carroll, P. Redlich, X. Blase, J.-C. Charlier, S. Curran, P. M. Ajayan, S. Roth, and M. Rühle, *Phys. Rev. Lett.* 81, 2332 (1998); (b) W. Han, Y. Bando, K. Kurashima, and T. Sato, *Chem. Phys. Lett.* 299, 368 (1999); (c) S. Peng and K. Cho, *Nano Lett.* 3, 513 (2003); (d) M. Zhao, Y. Xia, J. P. Lewis, and R. Zhang, *J. Appl. Phys.* 94, 2398 (2003); (e) A. V. Nikulkina and P. N. D'yachkov, *Russ. J. Inorg. Chem.* 49, 430 (2004).
20. (a) P. Lambin, A. A. Lucas, and J. C. Charlier, *J. Phys. Chem. Solids* 58, 1833 (1997); (b) H. J. Choi, J. Ihm, S. G. Louie, and M. L. Cohen, *Phys. Rev. Lett.* 84, 2917 (2000); (c) M. B. Nardelli, J.-L. Fattebert, D. Orlikowski, C. Roland, Q. Zhao, and J. Bernholc, *Carbon* 38, 1703 (2000); (d) H.-F. Hu, Y.-B. Li, and H.-B. He, *Diamond Rel. Mater.* 10, 1818 (2001); (e) L. G. Zhou and S. Q. Shi, *Carbon* 41, 579 (2003); (f) Y. Miyamoto, A. Rubio, S. Berber, M. Yoon, and D. Tománek, *Phys. Rev. B* 69, 121413 (2004).
21. (a) D. E. Clemmer, J. M. Hunter, K. B. Shelimov, and M. F. Jarrold, *Nature (London)* 372, 248 (1994); (b) W. Branz, I. M. L. Billas, N. Malinowski, F. Tast, M. Heinebrodt, and T. P. Martin, *J. Chem. Phys.* 109, 3425 (1998); (c) J. M. Poblet, J. Muñoz, K. Winkler, M. Cancilla, A. Hayashi, C. B. Lebrilla, and A. L. Balch, *Chem. Commun.* 493 (1999); (d) Q. Kong, Y. Shen, L. Zhao, J. Zhuang, S. Qian, Y. Li, Y. Lin, and R. Cai, *J. Chem. Phys.* 116, 128 (2002); (e) A. Hayashi, Y. Xie, J. M. Poblet, J. M. Campanera, C. B. Lebrilla, and A. L. Balch, *J. Phys. Chem. A* 108, 2192 (2004).
22. (a) C. Ding, J. Yang, X. Cui, and C. T. Chan, *J. Chem. Phys.* 111, 8481 (1999); (b) I. M. L. Billas, C. Massobrio, M. Boero, M. Parrinello, W. Branz, F. Tast, N. Malinowski, M. Heinebrodt, and T. P. Martin, *Comput. Mater. Sci.* 17, 191 (2000).
23. X. Blase, J.-C. Charlier, A. De Vita, and R. Car, *Appl. Phys. Lett.* 70, 197 (1996).
24. D. Golberg, Y. Bando, W. Han, K. Kurashima, and T. Sato, *Chem. Phys. Lett.* 308, 337 (1999).
25. S. L. Sung, S. H. Tsai, C. H. Tseng, F. K. Chiang, X. W. Liu, and H. C. Shih, *Appl. Phys. Lett.* 74, 197 (1999).
26. (a) A. Szabo and N. S. Ostlund, "Modern Quantum Chemistry." Dover, New York, 1996; (b) R. McWeeny, "Methods of Molecular Quantum Mechanics," 2nd Edn., Academic, New York, 1992; (c) F. Jensen, "Introduction to Computational Chemistry," Wiley, New York, 1998; (d) D. C. Young, "Computational Chemistry: A Practical Guide for Applying Techniques to Real World Problems," Wiley, New York, 2001; (e) C. J. Cramer, "Essentials of Computational Chemistry: Theories and Models," Wiley, New York, 2002.
27. (a) P. Hohenberg and W. Kohn, *Phys. Rev.* 136, B864 (1964); (b) W. Kohn and L. J. Sham, *Phys. Rev.* 40, A1133 (1965); (c) R. G. Parr and W. Yang, "Density-Functional Theory of Atoms and Molecules," Oxford University Press, New York, 1989; (d) Y. A. Wang and E. A. Carter, in "Theoretical Methods in Condensed Phase Chemistry" (S. D. Schwartz, Ed.), p. 117, Kluwer, Dordrecht, 2000.
28. C. C. J. Roothaan, *Rev. Mod. Phys.* 23, 69 (1951).
29. B. O. Roos, in "Advances in Chemical Physics: Ab Initio Methods in Quantum Chemistry Part II" (K. P. Lawley, Ed.), Vol. 69, p. 1, Wiley, New York, 1987.
30. I. Shavitt, in "Modern Theoretical Chemistry" (H. F. Sscaefer, Ed.), Vol. 3, p. 189, Plenum, New York, 1977.

31. J. Cizek, *J. Chem. Phys.* 45, 4256 (1966).
32. (a) J. A. Pople, D. P. Santry, and G. A. Segal, *J. Chem. Phys.* 43, S129 (1965); (b) J. A. Pople and G. A. Segal, *J. Chem. Phys.* 43, S136 (1965); (c) J. A. Pople and G. A. Segal, *J. Chem. Phys.* 44, 3289 (1966).
33. J. A. Pople, D. L. Beveridge, and P. A. Dobosh, *J. Chem. Phys.* 47, 2026 (1967).
34. M. J. S. Dewar and W. Thiel, *J. Am. Chem. Soc.* 99, 4899 (1977).
35. M. J. S. Dewar, E. G. Zoebisch, E. F. Healy, and J. J. P. Stewart, *J. Am. Chem. Soc.* 107, 3902 (1985).
36. (a) J. J. P. Stewart, *J. Comput. Chem.* 10, 209 (1989); (b) J. J. P. Stewart, *J. Comput. Chem.* 10, 221 (1989).
37. W. Kohn, A. D. Becke, and R. G. Parr, *J. Phys. Chem.* 100, 12974 (1996).
38. A. D. Becke, *J. Chem. Phys.* 98, 5648 (1993).
39. S. Dapprich, I. Komáromi, K. S. Byun, K. Morokuma, and M. J. Frisch, *J. Mol. Struct.* 461, 1 (1999).
40. (a) T. Klüner, N. Govind, Y. A. Wang, and E. A. Carter, *J. Chem. Phys.* 116, 42 (2002); (b) T. Klüner, N. Govind, Y. A. Wang, and E. A. Carter, *Phys. Rev. Lett.* 88, 209702 (2002); (c) T. Klüner, N. Govind, Y. A. Wang, and E. A. Carter, *Phys. Rev. Lett.* 86, 5954 (2001); (d) N. Govind, Y. A. Wang, and E. A. Carter, *J. Chem. Phys.* 110, 7677 (1999); (e) N. Govind, Y. A. Wang, A. J. R. da Silva, and E. A. Carter, *Chem. Phys. Lett.* 295, 129 (1998).
41. W. D. Cornell, P. Cieplak, C. I. Bayly, I. R. Gould, K. M. Merz, Jr., D. M. Ferguson, D. C. Spellmeyer, T. Fox, J. W. Caldwell, and P. A. Kollman, *J. Am. Chem. Soc.* 117, 5179 (1995).
42. B. R. Brooks, R. E. Bruccoleri, B. D. Olafson, D. J. States, S. Swaminathan, and M. Karplus, *J. Comp. Chem.* 4, 187 (1983).
43. N. L. Allinger, Y. H. Yuh, and J.-H. Lii, *J. Am. Chem. Soc.* 111, 8551 (1989).
44. A. K. Rappé, C. J. Casewit, K. S. Colwell, W. A. Goddard, III, and W. M. Skiff, *J. Am. Chem. Soc.* 114, 10024 (1992).
45. A. De Vita, J.-C. Charlier, X. Blasé, and R. Car, *Appl. Phys. A* 68, 283 (1999).
46. R. Tamura and M. Tsukada, *Phys. Rev. B* 52, 6015 (1995).
47. Gaussian 03, Revision B.05, M. J. Frisch, G. W. Trucks, H. B. Schlegel, G. E. Scuseria, M. A. Robb, J. R. Cheeseman, J. A. Montgomery, Jr., T. Vreven, K. N. Kudin, J. C. Burant, J. M. Millam, S. S. Iyengar, J. Tomasi, V. Barone, B. Mennucci, M. Cossi, G. Scalmani, N. Rega, G. A. Petersson, H. Nakatsuji, M. Hada, M. Ehara, K. Toyota, R. Fukuda, J. Hasegawa, M. Ishida, T. Nakajima, Y. Honda, O. Kitao, H. Nakai, M. Klene, X. Li, J. E. Knox, H. P. Hratchian, J. B. Cross, C. Adamo, J. Jaramillo, R. Gomperts, R. E. Stratmann, O. Yazyev, A. J. Austin, R. Cammi, C. Pomelli, J. W. Ochterski, P. Y. Ayala, K. Morokuma, G. A. Voth, P. Salvador, J. J. Dannenberg, V. G. Zakrzewski, S. Dapprich, A. D. Daniels, M. C. Strain, O. Farkas, D. K. Malick, A. D. Rabuck, K. Raghavachari, J. B. Foresman, J. V. Ortiz, Q. Cui, A. G. Baboul, S. Clifford, J. Cioslowski, B. B. Stefanov, G. Liu, A. Liashenko, P. Piskorz, I. Komaromi, R. L. Martin, D. J. Fox, T. Keith, M. A. Al-Laham, C. Y. Peng, A. Nanayakkara, M. Challacombe, P. M. W. Gill, B. Johnson, W. Chen, M. W. Wong, C. Gonzalez, and J. A. Pople, Gaussian, Inc., Pittsburgh, PA, 2003.
48. (a) J. P. Perdew, I. A. Chevary, S. H. Vosko, K. A. Jackson, M. R. Pederson, D. J. Singh, and C. Fiolhais, *Phys. Rev. B* 46, 6671 (1992); (b) J. P. Perdew, K. Burke, and Y. Wang, *Phys. Rev. B* 54, 16533 (1996).
49. (a) R. Ditchfield, W. J. Hehre, and J. A. Pople, *J. Chem. Phys.* 54, 724 (1971); (b) W. J. Hehre, R. Ditchfield, and J. A. Pople, *J. Chem. Phys.* 56, 2257 (1972); (c) P. C. Hariharan and J. A. Pople, *Mol. Phys.* 27, 209 (1974); (d) M. S. Gordon, *Chem. Phys. Lett.* 76, 163 (1980).
50. P. J. Hay and W. R. Wadt, *J. Chem. Phys.* 82, 299 (1985).
51. A. E. Reed, L. A. Curtiss, and F. Weinhold, *Chem. Rev.* 88, 899 (1988).
52. T. Yumura, S. Bandow, K. Yoshizawa, and S. Iijima, *J. Phys. Chem. B* 108, 11426 (2004).
53. (a) C. Lee, W. Yang, and R. G. Parr, *Phys. Rev. B* 37, 785 (1988); (b) B. Miehlich, A. Savin, H. Stoll, and H. Preuss, *Chem. Phys. Lett.* 157, 200 (1989).
54. W. Q. Tian and Y. A. Wang, *J. Org. Chem.* 69, 4299 (2004); (b) Y. Sheng, D. G. Musaev, K. S. Reddy, F. E. McDonald, and K. Morokuma, *J. Am. Chem. Soc.* 124, 4149 (2002); (c) L. Vereecken, J. Peeters, H. F. Bettinger, R. I. Kaiser, P. V. R. Schleyer, and H. F. Schaefer, III, *J. Am. Chem. Soc.* 124, 2781 (2002); (d) H. Jiao, G. Frapper, J.-F. Halet, and J.-Y. Saillard, *J. Phys. Chem. A* 105, 5945 (2001); (e) B. R. Beno, S. Wilsey, and K. N. Houk, *J. Am. Chem. Soc.* 121, 4816 (1999).

Handbook of
THEORETICAL and COMPUTATIONAL
NANOTECHNOLOGY

Edited by **Michael Rieth** and **Wolfram Schommers**

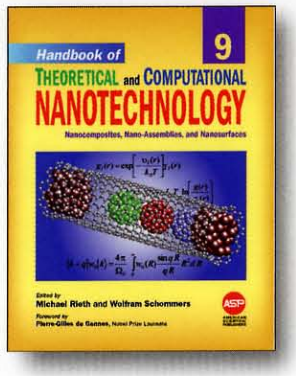

The future applications of nanotechnology in high-tech industries require deep understanding of the theoretical and computational aspects of all kinds of materials and devices on a nanometer scale. ***Handbook of Theoretical and Computational Nanotechnology*** is the first single reference source ever published in the field that offers such an unified approach, covering all of the major topics dealing with theory, modeling, design, and simulations of nanostructured materials and nanodevices, quantum computing, computational chemistry, physics, and biology, nanomechanics, nanomachines, nanoelectronics, nanoprocesses, nanomagnetism, nanooptics, nanomedicines, nanobiotechnology, etc. This 10-volume handbook provides the first ideal introduction and an up-to-date survey of the fascinating new developments and interdisciplinary activities in the whole field presented by scientists working in different subject areas of science, engineering, and medicine. This handbook is the most profound publication on this topic-the first treatment of computational nanotechnology. This outstanding handbook, presented by the world's leading scientists, is the most significant academic title ever published in this research field. This handbook has been divided into 10 thematic volumes by documenting computational treatment of nanomaterials and nanodevices.

Volume 1: Basic Concepts, Nanomachines, and Medical Nanodevices
Volume 2: Atomistic Simulations—Algorithms and Methods
Volume 3: Quantum and Molecular Computing, Quantum Simulations
Volume 4: Nanomechanics and Multiscale Modeling
Volume 5: Transport Phenomena and Nanoscale Processes
Volume 6: Bioinformatics, Nanomedicine, and Drug Design
Volume 7: Magnetic Nanostructures and Nanooptics
Volume 8: Functional Nanomaterials, Nanoparticles, and Polymer Design
Volume 9: Nanocomposites, Nano-Assemblies, and Nanosurfaces
Volume 10: Nanodevice Modeling and Nanoelectronics

KEY FEATURES

- The World's first handbook ever published in the field of theoretical and computational nanotechnology.
- The first comprehensive reference dedicated to all disciplines of science, engineering, and medicine.
- Most up-to-date reference source drawing on the past two decades of pioneering research.
- About 140 Review chapters written by world leading scientists familiar with the current trends of nanotechnology.
- Over 8,000 pages written by 265 authors from 30 countries, truly international.
- 26,000 references, 4124 figures, 374 tables, and thousands of mathematical equations and formula.
- Clearly written, self-contained, timely, authoritative, and most comprehensive contributions.
- Extensive cross-refereeing in each chapter provides reader with a broader range of knowledge.
- Multidisciplinary reference source for scientists, engineers, biologists, medical experts and related professionals.

READERSHIP

This handbook is an invaluable reference source for scientists, engineers, and biologists working in the field of theoretical and computational nanotechnology. The handbook is intended for a broad audience working in the fields of quantum chemistry, physics, biology, materials science, electrical and electronics engineering, mechanical engineering, optical science, ceramic and chemical engineering, device engineering, aerospace engineering, computer science and technology, information technology, bioinformatics, biotechnology, medical sciences, medicine, surface science, and polymer science and technology.

ISBN 1-58883-051-9
9 781588 830517 90000

ASP **AMERICAN SCIENTIFIC PUBLISHERS**
Los Angeles, California, USA

Printed in the United States of America